DEEP INELASTIC SCATTERING AT HERA*

G. WOLF

Deutsches Elektronen Synchrotron DESY
Notkestr. 85, Hamburg 52, Germany

(Received November 12, 1997)

Precise $\mathcal{F}_2$ measurements have been performed in deep inelastic (DIS) e^+p scattering by H1 and ZEUS over a wide range in x from 10^{-5} to 0.3 and in Q^2 from 0.16 to 5000 GeV^2. $\mathcal{F}_2$, as well as the gluon momentum density $xg(x,Q^2)$, extracted from $d\mathcal{F}_2/d\ln Q^2$ exhibit a fast rise as $x \to 0$ which shows that the proton's quark and gluon densities at small x are large. The data on $\mathcal{F}_2$ as well as the first measurements of the longitudinal structure function $\mathcal{F}_L$ and the charm contribution to $\mathcal{F}_2$ are in agreement with DGLAP evolution. Comparison of results obtained for very small values of Q^2 with theoretical models suggests that for $x < 10^{-2}$ the transition from soft to hard scattering occurs at Q^2 values below $\approx$ 1 GeV^2. The DIS NC and CC measurements have been extended to large values of $Q^2 \approx M_W^2, M_Z^2$. For Q^2 above M_W^2 the weak force is found to have similar strength as the electromagnetic one. Combining e^+p data from 1994–97 running for a total integrated luminosity of 58 pb^{-1} H1 and ZEUS have observed an excess of NC events over the predictions of the Standard Model (SM) for $Q^2 > 15000$ GeV^2. The excess occurs at large x corresponding to large masses M of the $e - hadron$ system, M around 200–230 GeV. The statistical probability that the data are compatible with the SM is at the 0.2–1% level. The data are compared with expectations for contact interactions, leptoquarks and squarks.

PACS numbers: 13.40. –f

1. The HERA collider and the experiments

The HERA collider can store electrons (positrons) of up to 30 GeV and protons of up to 820 GeV in two rings of 6.3 km circumference [1]. Table I lists some of the salient parameters of the machine. In order to maximize the luminosity up to 210 bunches of particles can be stored for each beam.

* Presented at the XXXVII Cracow School of Theoretical Physics Zakopane, Poland, May 30–June 10, 1997.

The time interval between consecutive bunches is 96 ns. The measured specific luminosity is almost a factor of two larger compared to the design value. The maximum peak luminosity achieved so far corresponds to about 90% of the design value. The integrated luminosity provided by HERA for e-p collisions during the running periods starting in 1992 is diplayed in Fig. 1. The total yearly luminosity increased by about a factor of two every year. With the present machine configuration a yearly luminosity of 30–40 pb^{-1} per experiment can be expected. An upgrade program has been started which promises a factor of 3–5 increase by the insertion of additional magnets close to the interaction point. HERA is expected to operate in the new configuration starting in the year 2000. An increase of the maximum beam energies is under study.

TABLE I

HERA machine parameters.

parameter	electron ring	proton ring
circumference (m)	6336	
energy (GeV)	30	820
$e-p$ c.m. energy (GeV)	314	
magn. bending field (T)	0.164	4.682
bend. radius dipoles (m)	610	584
max. circ. curr. design (mA)	60	160
max. circ. curr. achiev.(mA)	40	100
n. part./beam design	$0.8 \cdot 10^{13}$	$2.1 \cdot 10^{13}$
n. bunch buckets	220	220
n. bunches	210	210
time betw. cross. (ns)	96	
max. lumi. design $10^{31} cm^{-2} s^{-1}$	1.5	
max. lumi. achiev. $10^{31} cm^{-2} s^{-1}$	1.4	
e polariz.	50–70%	

HERA has four interaction regions. The general purpose detectors H1 [2] and ZEUS [3] study the interactions between the electron (positron) and proton colliding beams. The HERMES collaboration measures the spin structure of nucleons by the interaction of the polarized electron (positron) beam with polarized nucleons (nuclei) of a gas-jet target [5]. In the HERA-B experiment CP violation in the $b\bar{b}$ system will be investigated by colliding protons from the halo of the 820 GeV proton beam with a fixed target [6]. Data taking with HERA-B is expected to start in 1998/99.

Figure 1 shows the yearly accumulated luminosity provided by HERA per experiment. Since the beginning of operation in summer of 1992 the yearly luminosity has increased steadily reaching 17 pb^{-1} in 1996 and 36

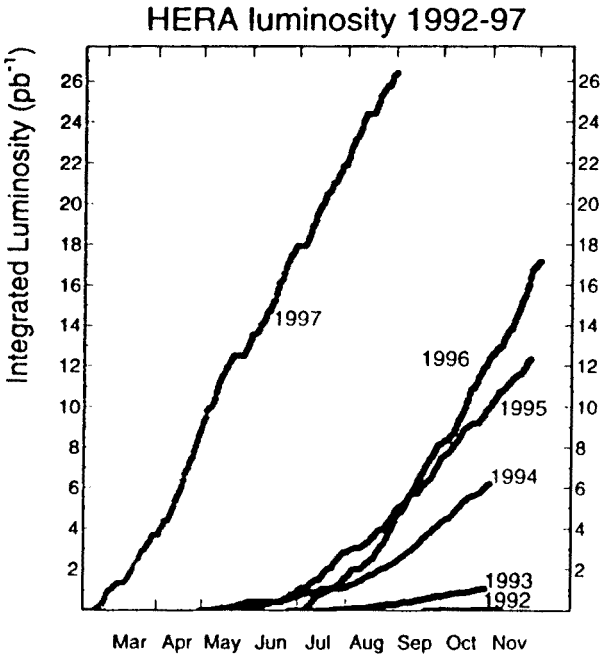

Fig. 1. Integrated yearly luminosity delivered by HERA for H1 and ZEUS per experiment during 1992 to 1996 and in the first months of 1997.

pb^{-1} in 1997. Also, the two experiments are continuously improving their efficiency of data taking. In 1997, data have been logged for about 70–85% of the luminosity delivered by HERA.

The H1 and ZEUS experiments have taken data with 26.7 GeV e^- on 820 GeV p (1992–3 running, integrated luminosity per experiment ≈ 0.6 pb^{-1}), 27.5 GeV e^- on 820 GeV p (1994, ≈ 0.3 pb^{-1}) and 27.5 GeV e^+ on 820 GeV p (1994–6, $\approx$ 14–20 pb^{-1} and 10–14 pb^{-1} during the first part of 1997).

The majority of the results presented below have been obtained from data taken during 1994 corresponding to an integrated luminosity of about 2.5 pb^{-1}. For the study of deep inelastic scattering at very large Q^2 and high x the data taken up until summer of this year have been included.

Figures 2 show two high Q^2 events of the type $e^+p \rightarrow e$+hadrons recorded by the H1 and ZEUS detectors. The high energy jet and the scattered positron are back-to-back in the transverse plane and balance transverse momentum as expected for neutral current events. The almost complete solid angle coverage (*e.g.* the ZEUS calorimetric coverage is 99.7%) allows reconstruction of the complete final state, except for particles which escape through the forward or rear beam holes.

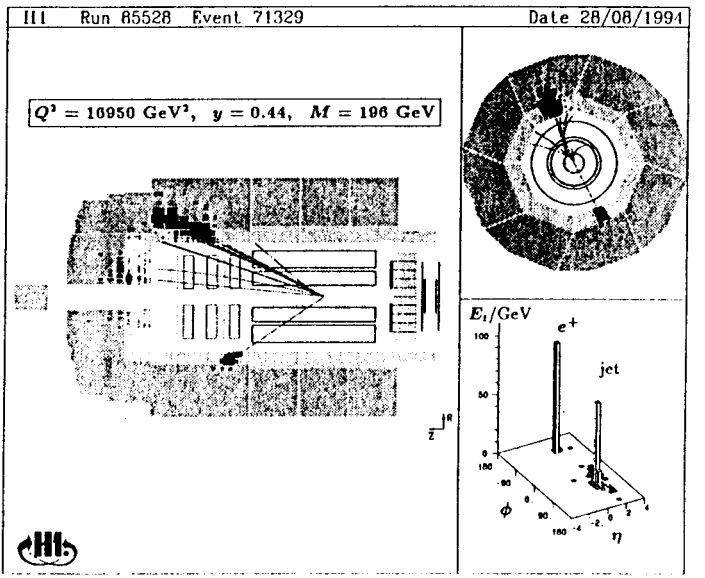

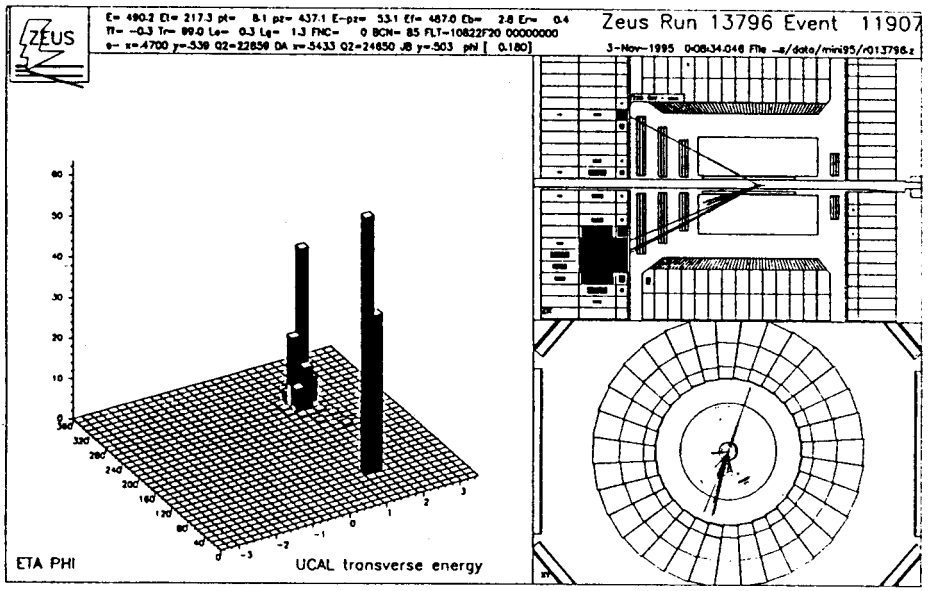

Fig. 2. Top: A DIS–NC event with $Q^2 = 17 \cdot 10^3$ GeV^2, $x = 0.43$ observed in the H1 detector.The e beam enters from the left, the p beam from the right.
Bottom: A DIS–NC event with $Q^2 = 25 \cdot 10^3$ GeV^2, $x = 0.57$ observed in the ZEUS detector. The e beam enters from the left, the p beam from the right.

2. Structure functions of the proton

Inclusive DIS,

$$e(k) + p(P) \to e'(k') + \text{anything}\,,$$

can be described as function of Bjorken-x and Q^2. The basic quantities, in the absence of QED radiation, are:

$$s = 4E_e E_p\,, \tag{1}$$

$$Q^2 = -q^2 = -(e - e')^2\,, \tag{2}$$

$$x = \frac{Q^2}{2P\,q}\,, \tag{3}$$

$$\nu = \frac{q\,P}{M_p}\,, \tag{4}$$

$$y = \frac{q\,P}{e\,P}\,, \tag{5}$$

$$Q^2 = x\,y\,s\,, \tag{6}$$

$$W^2 = \frac{Q^2(1-x)}{x} + M_p^2 \approx \frac{Q^2}{x} \quad \text{for } x \ll 1\,, \tag{7}$$

where e and e' are the four-momenta of the initial and final state electrons, P is the initial state proton four-momentum, M_p is the proton mass, s is the square of the ep c.m. energy, ν is the energy transfer and y the fractional energy transfer from the incident electron to the proton as measured in the proton rest frame, $y = \nu/\nu_{\max}$, $\nu_{\max} = s/(2M_p)$, and W is the $\gamma^* p$ c.m. energy.

The proton structure function F_2 has been measured at HERA over a wide range in x and Q^2 as shown in Fig. 3. At large x the HERA data overlap with those obtained by fixed target experiments. Special runs where the collision points in H1 and ZEUS have been moved by about 70 cm as well as the installation of special calorimeters close to the beams have allowed to extend the measurements into the transition region from photoproduction to DIS. Precise results on the NC proton structure function $\mathcal{F}_2$ are available from the 1994 running period from H1 [7] (integrated luminosity 2.7 pb^{-1}, 240 kevents) and ZEUS [8,9] (2.6 pb^{-1}, 380 kevents).

The differential cross section for deep inelastic scattering DIS can be expressed in terms of three structure functions, $\mathcal{F}_2, \mathcal{F}_\mathrm{L}, \mathcal{F}_3$ [51]:

$$\frac{d^2\sigma}{dx dQ^2} = \frac{2\pi\alpha^2}{xQ^4}[(1 + (1-y)^2)\mathcal{F}_2 - y^2\mathcal{F}_\mathrm{L} \pm (1 - (1-y)^2)x\mathcal{F}_3]\,, \tag{8}$$

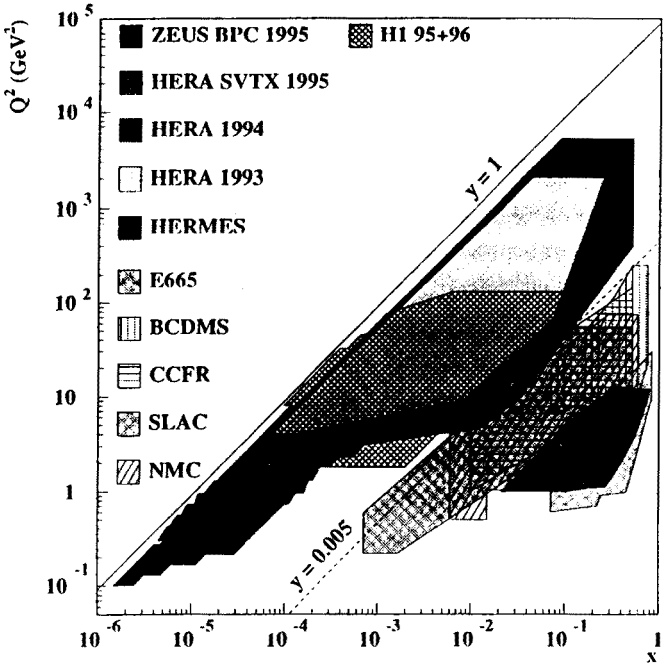

Fig. 3. The x–Q^2 plane: the regions covered by H1 and ZEUS and by fixed target experiments.

where α is the fine structure constant and the upper (lower) sign applies to e^- (e^+) p scattering. Since the contributions from $\mathcal{F}_L$ and $\mathcal{F}_3$ are expected to be small in the measured region, the radiatively corrected NC cross section can be written as:

$$\frac{d^2\sigma}{dxdQ^2} = \frac{2\pi\alpha^2}{xQ^4}[(1+(1-y)^2)\mathcal{F}_2](1-\delta_L-\delta_3)\,. \tag{9}$$

The structure function $\mathcal{F}_2$ receives contributions from photon and Z^o exchange and can be written as

$$\mathcal{F}_2 = F_2^{em}(1+\delta_Z). \tag{10}$$

The corrections $\delta_{Z,L,3}$ are functions of x and Q^2 but are, to a good approximation, independent of $\mathcal{F}_2$, *i.e.* they are insensitive to the parton density distributions. They were calculated from theory using structure functions which gave a good representation of the data. In the measured region δ_L is small except when $y \geq 0.7$ where $\delta_L \approx 0.12$. The contributions from $\delta_{Z,3}$ are negligible for $Q^2 < 1000$ GeV^2. They reach at

$$Q^2 = 3000\text{GeV}^2,\ x = 0.08(0.20):\ \delta_Z = 0.05(0.04),\ \delta_3 = 0.08(0.05),$$

and at

$$Q^2 = 5000\text{GeV}^2,\ x = 0.08(0.20):\ \delta_Z = 0.08(0.075),\ \delta_3 = 0.22(0.11).$$

In QCD, ignoring the contributions from Z^o exchange, $\mathcal{F}_2$ can be expressed in terms of the quark densities $q(x, Q^2)$ of the proton:

$$\mathcal{F}_2 = \sum_q e_q^2 x q(x, Q^2)\,, \tag{11}$$

where e_q is the electric charge of quark q.

2.1. Structure function $\mathcal{F}_2$

The results on $\mathcal{F}_2$ from H1 and ZEUS are presented in Figs. 4. The error bars show the statistical and systematic uncertainties added in quadrature. For $Q^2 < 100$ GeV^2 the typical statistical and systematic errors are 2–5% and 3–6%, respectively. There is good agreement between the two HERA experiments. Also shown are the data from the fixed target experiments: BCDMS [10], E665 [11], NMC [12] and SLAC [13] which cover the region of '*large*' x. In the region, where the HERA and the fixed target data overlap, good agreement is observed.

The most striking feature of the HERA data is the rapid rise of $\mathcal{F}_2$ as $x \to 0$ which is seen to persist down to Q^2 values as small as 1.5 GeV^2. The rise accelerates with increasing Q^2 as shown by Fig. 5 where ZEUS data from $Q^2 = 10$, 22, 90 and 250 GeV^2 have been overlaid. Some insight can be gained by fitting these data to the form $\mathcal{F}_2 = a + bx^{-\lambda}$. The (preliminary) fit results are given in Table II. The contribution from the constant term a is found to decrease rapidly with Q^2. The power λ of the x dependent term is rather constant with Q^2 while the coefficient b rises for Q^2 between 10 and 90 GeV^2 and appears to be driving the rapid rise of $\mathcal{F}_2$.

TABLE II

Parameters from the fit of ZEUS $\mathcal{F}_2$ data to the form $\mathcal{F}_2 = a + bx^{-\lambda}$, preliminary.

parameter	Q^2=10GeV^2	22GeV^2	90GeV^2	250GeV^2
a	0.31±0.03	0.14±0.05	0.01±0.11	0.06±0.11
b	0.05±0.01	0.10±0.02	0.18±0.07	0.11±0.06
λ	0.36±0.02	0.32±0.02	0.32±0.05	0.44±0.10

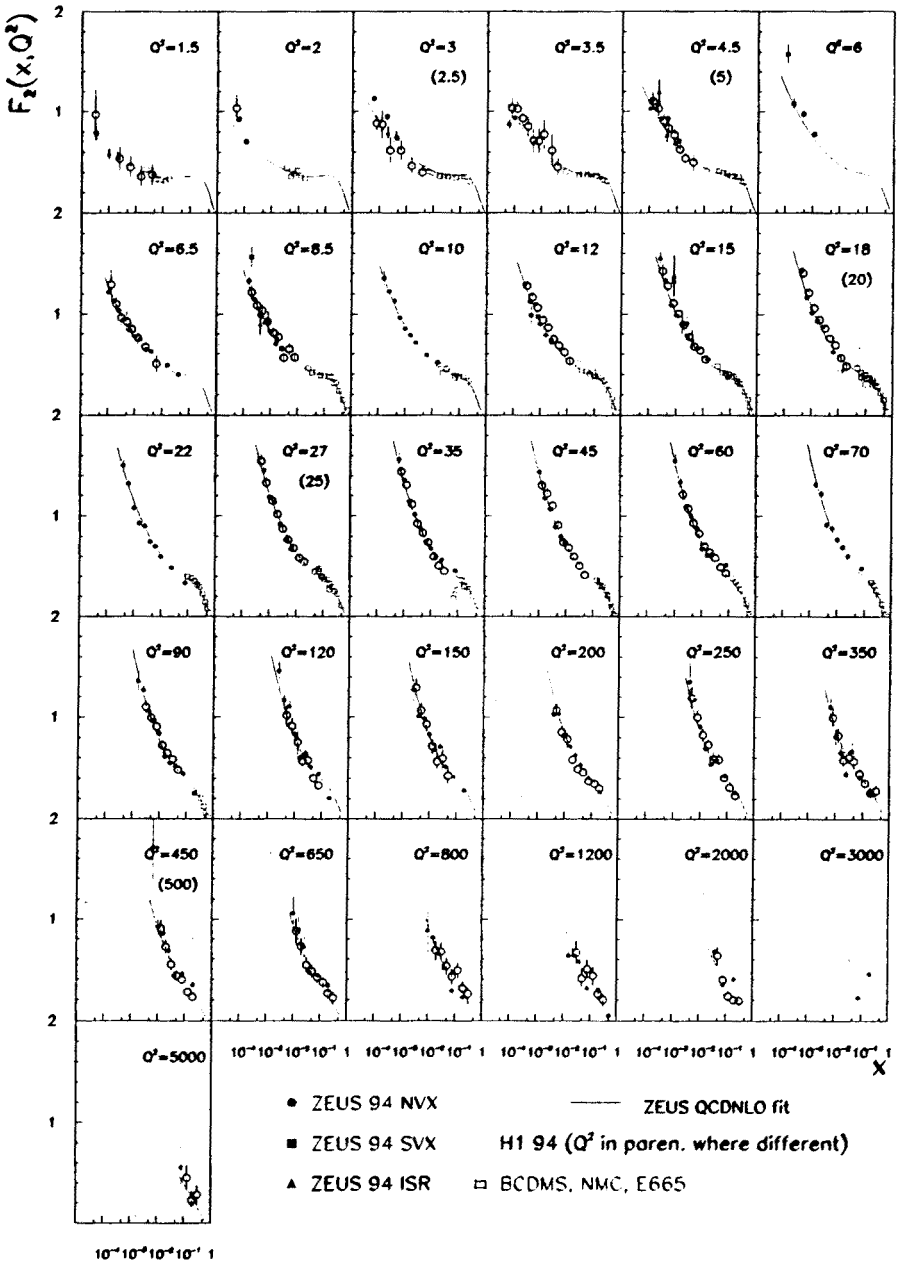

Fig. 4. Structure function $\mathcal{F}_2$ from NC scattering as a function of x for fixed values of Q^2 as measured by H1, ZEUS. Also shown are the data from the fixed target experiments BCDMS, E665, NMC and SLAC. The solid lines indicate a QCD NLO fit to the data from ZEUS and NMC.

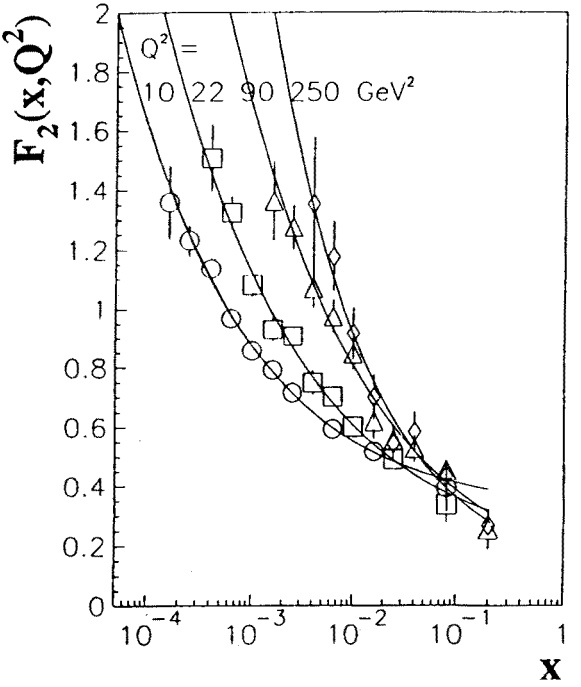

Fig. 5. Structure function $\mathcal{F}_2$ from NC scattering as a function of x for fixed values of $Q^2 = 10$, 22, 90 and 250 GeV^2 as measured by ZEUS.

Fits performed without a constant term ($a \equiv 0$) result in considerably larger values of χ^2/ndf for $Q^2 < 40$ GeV^2. Thus, in this range of Q^2 the data indicate the presence of a soft term $a \neq 0$ as has been noticed before [4]. If a is set to zero λ is found to rise with Q^2, see *e.g.* [7].

Figure 6 shows the $\mathcal{F}_2$ values as a function of Q^2 for fixed x. Scaling violations proportional to $\ln Q^2$ are observed which decrease as x increases. For $x > 0.01$ the data now span three decades in Q^2.

The curves shown in Figs 4, 6 give the result of a QCD NLO fit based on the DGLAP evolution [14] to the combined ZEUS and NMC data. The fit shows that NLO DGLAP evolution can give a consistent description of the data over the full Q^2 range.

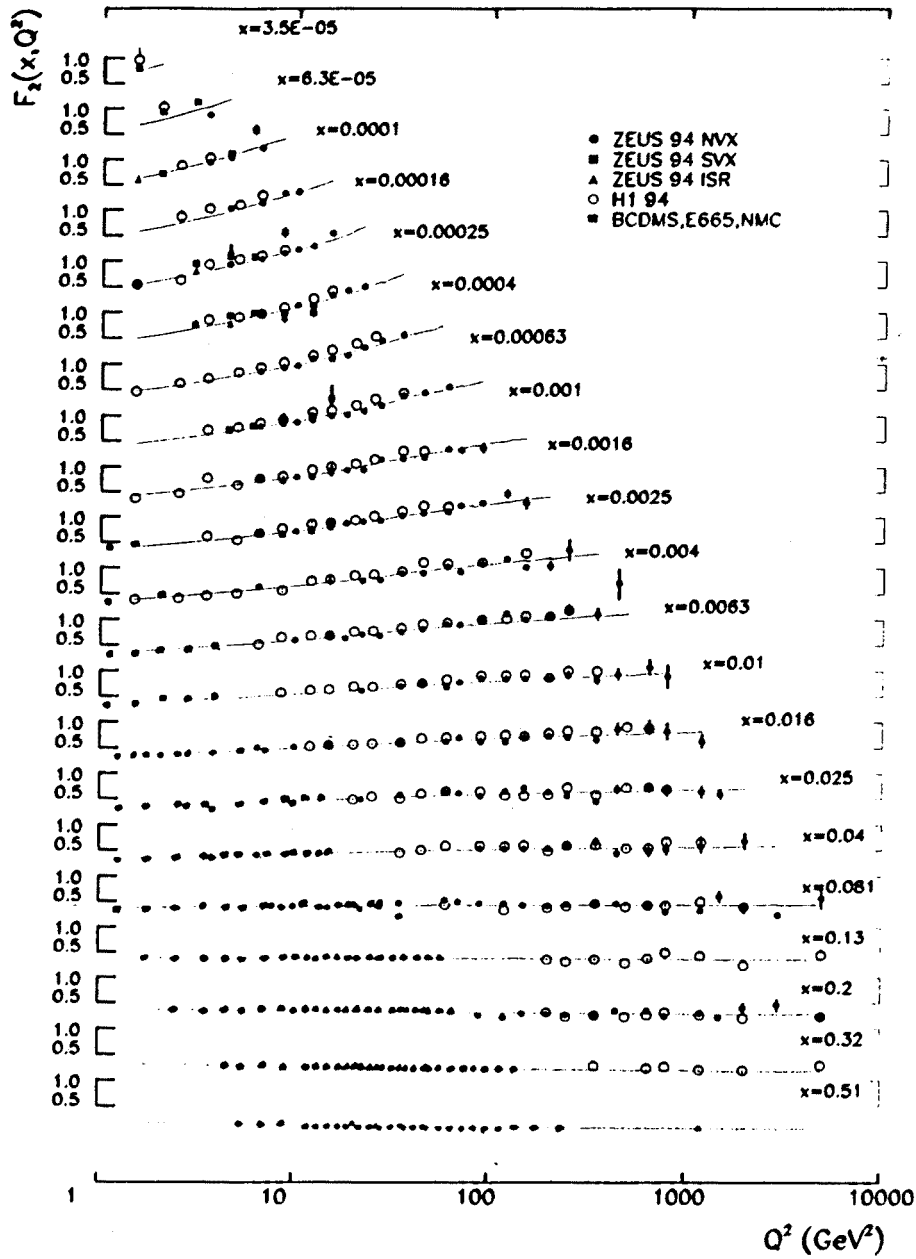

Fig. 6. Structure function $\mathcal{F}_2$ from NC scattering as a function of Q^2 for fixed values of x as measured by H1, ZEUS. Also shown are the data from the fixed target experiments BCDMS, E665, NMC and SLAC. The solid lines indicate a QCD NLO fit to the data from ZEUS and NMC.

2.2. Structure function $\mathcal{F}_L$

In the Quark Parton Model (QPM = zero order QCD), $\mathcal{F}_L$ vanishes for spin 1/2 partons. In LO QCD $\mathcal{F}_L$ acquires a nonzero value due to the contribution from gluon radiation which is proportional to the strong coupling constant α_s. A direct determination of $\mathcal{F}_L$ requires the measurement of the DIS cross section at fixed x, Q^2 for different values of y which can be accomplished *e.g.* by varying the ep c.m. energy squared s.

H1 has shown that for a limited region of high y, $\mathcal{F}_L$ can be extracted from the $\mathcal{F}_2$ measurements at a single value of s if these are combined with a rather weak assumption on the validity of the DGLAP evolution [15]. At high y the factors $1+(1-y)^2$ and y^2 which multiply $\mathcal{F}_2$ and $\mathcal{F}_L$, respectively, in the expression for the DIS cross section (see Eq. (8)), become of comparable magnitude. With this in mind, the following procedure was chosen. The $\mathcal{F}_2$ values measured by H1 for $y < 0.35$ and by BCDMS at larger values of x are used to extract the parton distribution functions. The DGLAP equations allow to evolve the parton distribution functions in Q^2 for fixed x and to predict $\mathcal{F}_2$ at high y. Subtraction of the $\mathcal{F}_2$ contribution yields then $\mathcal{F}_L$. Note, as shown above, NLO DGLAP gives a good description of the $\mathcal{F}_2$ data over four orders of magnitude in x and Q^2, while for the determination of $\mathcal{F}_L$ the evolution extends the maximum Q^2 at fixed x by only a factor of two. Nevertheless, this analysis can not strictly exclude the possibility that $\mathcal{F}_2$ behaves differently than assumed.

The longitudinal structure function $\mathcal{F}_L$ extracted in this manner is shown in Fig. 7 as a function of Q^2 or $x = Q^2/(sy)$ at $y = 0.7$. The full error bars represent the statistical and systematic uncertainties added in quadrature. The $\mathcal{F}_L$ values are significantly above zero and a factor of 2–3 below those of $\mathcal{F}_2$. The dashed band, which shows $\mathcal{F}_L$ as expected from the QCD NLO analysis, is consistent with the extracted $\mathcal{F}_L$ values.

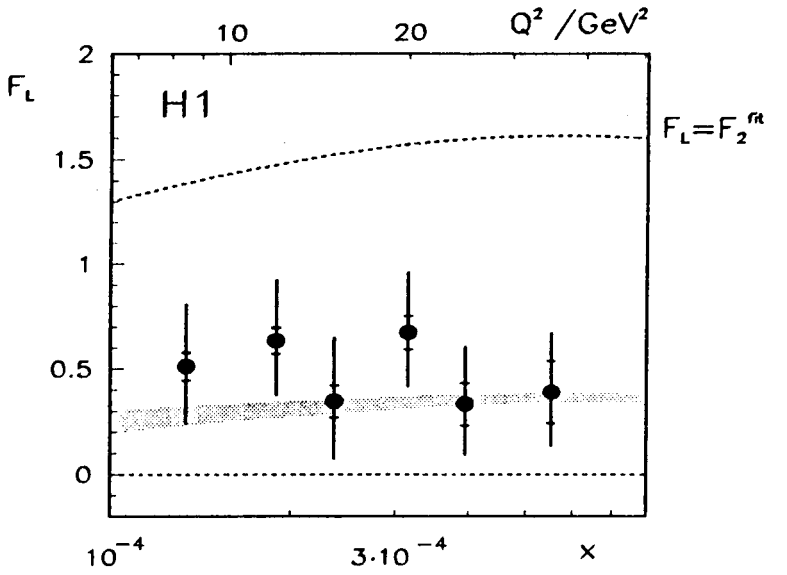

Fig. 7. Structure function $\mathcal{F}_{\mathrm{L}}$ from NC scattering as a function of Q^2 or $x = Q^2/(sy)$ at $y = 0.7$ as determined by H1. The full error bars show the statistical and systematic errors added in quadrature. The dashed band shows $\mathcal{F}_{\mathrm{L}}$ as expected from the QCD NLO analysis.

2.3. Gluon density of the proton

In QPM the structure functions scale. Scaling violations arise from QCD radiative effects which in LO have a simple mathematical expression:

$$\frac{d\mathcal{F}_2}{d\ln Q^2} = \sum_q e_q^2 \frac{\alpha_s(Q^2)}{2\pi} \int_x^1 \frac{dy}{y} [P_{qq}\left(\frac{x}{y}\right) q(y,Q^2) + P_{qg}\left(\frac{x}{y}\right) g(x,Q^2)]. \quad (12)$$

Here, P_{qq} and P_{qg} are the quark and gluon splitting functions and $g(x,Q^2)$ is the gluon density of the proton. At small x, $x < 10^{-2}$, the dominant contribution is expected to come from quark-pair creation by gluons (second term in Eq. (12)) which offers the possibility to determine the density of gluons in the proton rather directly. Figure 8 shows the gluon momentum density $xg(x,Q^2)$ versus x for fixed Q^2 as determined by H1 [7] from NLO fits to the $\mathcal{F}_2$ data. The dashed bands show the estimated uncertainties.

The gluon momentum density is seen to rise rapidly as $x \to 0$ for fixed Q^2 and with increasing Q^2 for fixed x.

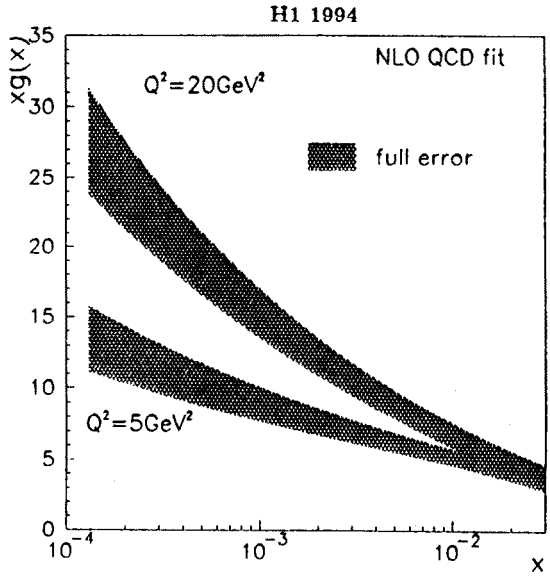

Fig. 8. The gluon momentum density of the proton as a function of x for fixed $Q^2 = 5$ and 20 GeV^2 as determined from NLO fits to the $\mathcal{F}_2$ data by H1. The bands show the estimated uncertainties.

It is instructive to convert the low x HERA data for $\mathcal{F}_2$ and $xg(x, Q^2)$ which give the quark plus antiquark and gluon momentum densities, respectively, into the number of partons in the proton and compare these with those obtained at large x by [16] from the parton density set MRSD0'. The result is shown in Table III. In the low x interval the number of $q, \overline{q}$ is a factor of about 4 above the value at large x and the number of gluons has risen by about a factor of 15.

TABLE III

Equivalent number of partons in the proton for $Q^2 = 20$ GeV^2 at low x determined from the H1 and ZEUS data and at large x from the MRSD0' set.

	$x > 0.06$	$5 \cdot 10^{-4} < x < 5 \cdot 10^{-3}$
$N_{q,\overline{q}}$	≈ 2.4	9 ± 1
N_g	≈ 1.8	27 ± 2

2.4. Charm contribution to $\mathcal{F}_2$

The structure function $\mathcal{F}_2$ measures the momentum densities of quarks in the proton summed over all quark flavors. H1 [17] and ZEUS [18] determined the cross section for charm production in DIS via the observation of D^* and D^0 mesons. Charmed particles are expected to be produced in DIS predominantly by virtual photon gluon fusion (BGF). Accordingly, the cross sections which where determined in a restricted kinematical region, where extrapolated to the full phase space using the BGF model.

The charm contribution $\mathcal{F}_2^{c\bar{c}}$ to $\mathcal{F}_2$ as obtained by H1 and ZEUS between $x = 3 \cdot 10^{-4}$ and 10^{-2} and Q^2 between 7 and 45 GeV^2 is shown in Fig. 9 together with the data from EMC measured at large x. The comparison between the HERA and EMC data shows that $\mathcal{F}_2^{c\bar{c}}$ rises rapidly as x decreases. One finds for the HERA data that at $Q^2 = 25$ GeV^2 charm contributes about 20 to 30% of the proton structure function $\mathcal{F}_2$. The GRV predictions [19, 20] which were calculated in NLO treating charm quarks as massive [21] are shown by the solid curves. They appear to be somewhat lower than the data.

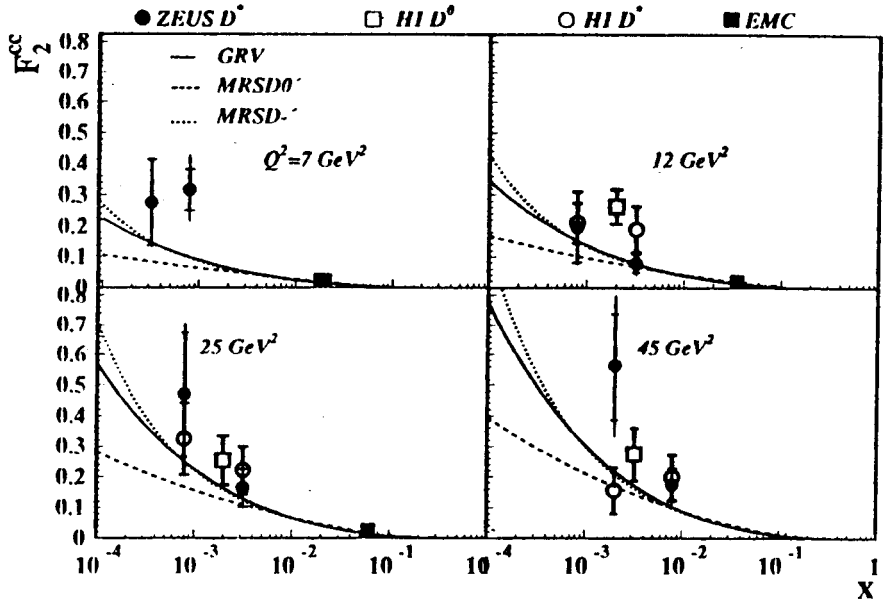

Fig. 9. The charm contribution $\mathcal{F}_2^{c\bar{c}}$ to the proton structure function as derived from inclusive D^* (H1 and ZEUS) and D^o (H1 and EMC analyses) for $Q^2 = 7$, 12, 25 and 45 GeV^2. Also shown are the NLO predictions based on GRV and MRSD0' parton distributions using a charm mass of $m_c = 1.5$ GeV.

2.5. $\mathcal{F}_2$ and the predictions of QCD

The DGLAP equations describe the evolution of the parton densities with Q^2. In order to solve these equations one must provide the parton densities as a function of x at some reference scale Q_0^2 which should be large enough for perturbative QCD to be applicable [22]. Assuming a Regge-type behavior [23,24], the small x dependence of the valence quark (v), sea quark (s) and gluon densities is of the form:

$$xq_{\rm v}(x,Q^2) \propto x^{1-\alpha_{\rm R}}\,, \tag{13}$$

$$xq_{\rm s}(x,Q^2) \propto x^{1-\alpha_{I\!P}}\,, \tag{14}$$

$$xg(x,Q^2) \propto x^{1-\alpha_{I\!P}}\,, \tag{15}$$

where α_R and $\alpha_{I\!P}$ denote the intercepts of the reggeon and pomeron trajectories. For $\alpha_{\rm R} \approx 0.5$ and $\alpha_{I\!P} \approx 1$ one obtains $xq_{\rm v}(x,Q_0^2) \propto x^{0.5}$ and $xq_{\rm s}(x,Q_0^2) \propto xg(x,Q_0^2) \propto$ const.. In the leading log Q^2 approximation the $x^{0.5}$ behavior of the valence distribution remains unchanged by the Q^2 evolution while the sea quark and gluon distributions at small x become steeper. In fact, in perturbative QCD, $\mathcal{F}_2$ is expected to grow faster than any power of $\ln(1/x)$ as $x \to 0$ [25,26]:

$$\mathcal{F}_2(x,Q^2) \approx C_0\Big[\frac{33-2n_f}{576\pi^2 \ln(1/x)\ln[\alpha_s(Q_0^2)/\alpha_s(Q^2)]}\Big]^{1/4} \times \exp\sqrt{\frac{144\ln(1/x)}{33-2n_f}\ln[\alpha_s(Q_0^2)/\alpha_s(Q^2)]}. \tag{16}$$

where n_f is the number of quark flavors. The rise of $\mathcal{F}_2$ as $x \to 0$ can be accelerated by decreasing the reference scale Q_0^2. This can be seen by applying Eq. (16) for a specific set of parameters, *e.g.* $n_f = 3$, $\alpha_s(Q^2) = 4\pi/(11-\frac{2}{3}n_f)\ln Q^2/\Lambda^2$ with $\Lambda = 0.2$ GeV. Starting with x-independent parton distributions at Q_0^2 and parametrizing the $\mathcal{F}_2(x,Q^2)$ values obtained from Eq. (16) as $\mathcal{F}_2(x,Q^2) = b(Q^2)(1/x)^{\lambda(Q^2)}$ for $10^{-4} < x < 10^{-2}$ yields

with $Q_0^2 = 4$ GeV^2 at $Q^2 = 10$ (20, 100)GeV^2: $\lambda \approx 0.15$ (0.21, 0.29)

with $Q_0^2 = 1$ GeV^2 at $Q^2 = 10$ (20, 100)GeV^2: $\lambda \approx 0.29$ (0.32, 0.38).

The DGLAP scheme of evolution requires angular ordering and neglects terms proportional to $\ln(1/x)$, an approximation, which may run in difficulties as $x \to 0$. The BFKL formalism [27] does not impose angular ordering and resums terms proportional to $\ln(1/x)$. Based on the BFKL formalism which performs QCD evolution for fixed Q^2 as function of x the gluon density in the proton was predicted to rise as $g(x,Q^2) \propto x^{-(1+\lambda)}$ as $x \to 0$,

where $\lambda \approx \alpha_s(12/\ln 2)/\pi \approx 0.5$ for $Q^2 = 20$ GeV^2. In BFKL-type calculations in NLO predict a considerably smaller value for λ, $\lambda \approx 0.15$ [28–30]. BFKL inspired fits to the data have been performed by [31].

The rapid rise of $\mathcal{F}_2$ at small x observed by the HERA experiments was anticipated in the GRV model [20] where a very small evolution scale, viz. $Q_0^2 = 0.34$ GeV^2, was chosen. The GRV predictions in NLO are compared with the experimental data on $\mathcal{F}_2$ data in Fig. 10 together with the NLO parametrizations of the parton densities MRSA' [32] and CTEQ3 [33]. At large Q^2 GRV and the parametrizations represent the data well. At $Q^2 \leq 18$ GeV^2 and $x < 10^{-3}$ GRV overshoots the data: a slight increase of Q_0^2 presumably can improve the agreement.

The authors of [23] in 1980 presented a NLO QCD model which predicted the rise of $\mathcal{F}_2$ at small x observed at HERA with remarkable accuracy. According to the model, $\mathcal{F}_2$ should behave at small x as a power in x, $\mathcal{F}_2 \propto x^{-\lambda_s}$ with λ_s being independent of Q^2, except for heavy flavor thresholds. Extending the scanty data available then down to $x \approx 0.05$ led to the prediction $\lambda_s = 0.37 \pm 0.07$. Adding a constant term to $\mathcal{F}_2$ a fit of the model to the new data from H1 and ZEUS provided a good description of the measurements and yielded $\lambda_s = 0.355 \pm 0.01$ [34]. Dividing the data into different Q^2 intervals indicated a possible but small rise of λ_s with Q^2 from 0.325 ± 0.01 at $Q^2 < 10$ GeV^2 to 0.355 ± 0.01 at $Q^2 > 100$ GeV^2.

Double-logarithmic scaling of $\mathcal{F}_2$ with respect to x and Q^2 has been investigated in [35, 36]. The rise observed in the HERA data at small x is consistent with a logarithmic rise in x as well as in Q^2. An economical parametrization which decribes the $\mathcal{F}_2$ data of H1 and ZEUS for $Q^2 \geq 0.11$ GeV^2 has been obtained in [37]:

$$\mathcal{F}_2(x, Q^2) = m \log_{10}\left(1 + \frac{Q^2}{Q_0^2}\right) \log_{10}\left(\frac{x_0}{x}\right) \tag{17}$$

with $Q_0^2 = 0.55$ GeV^2, $x_0 = 0.04$ and $m = 0.45$.

2.6. The small x behaviour of $\mathcal{F}_2$ and the W dependence of $\sigma^{\mathrm{tot}}_{\gamma^* p}$

Neglecting contributions from Z^0 exchange, the DIS cross section can be expressed in terms of the flux of virtual photons times the total cross section for virtual - photon proton scattering, $\sigma^{\mathrm{tot}}_{\gamma^* p}$ [38]. $\sigma^{\mathrm{tot}}_{\gamma^* p}$ is defined in terms of the cross sections for the scattering of transverse and longitudinal photons,

$$\sigma^{\mathrm{tot}}_{\gamma^* p}(x, Q^2) = \sigma_{\mathrm{T}}(x, Q^2) + \sigma_{\mathrm{L}}(x, Q^2). \tag{18}$$

The cross section defined in this manner can be interpreted in a way similar to the case of the interaction of real photons provided the lifetime of the

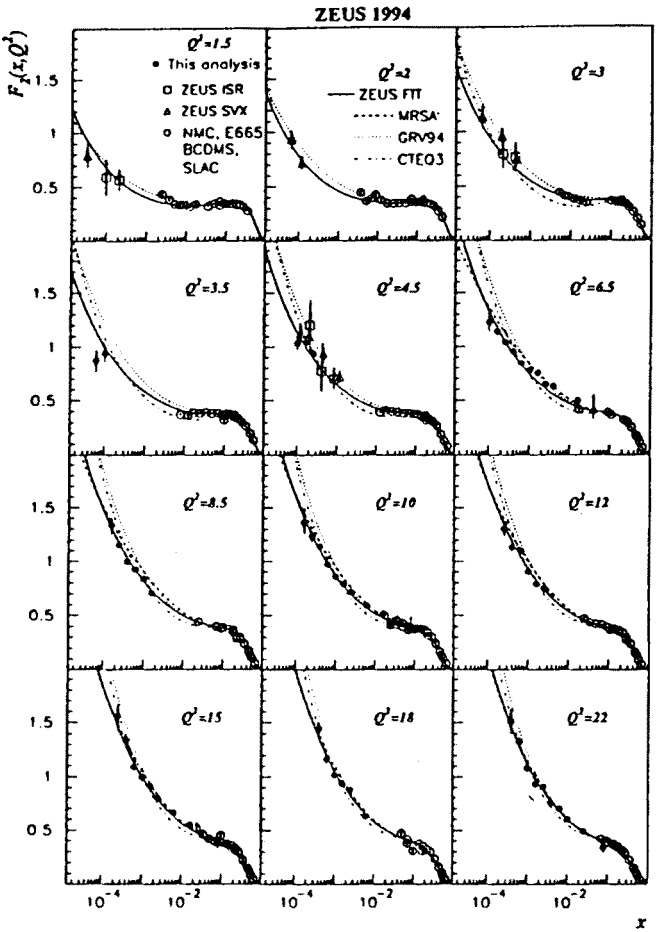

Fig. 10. Structure function $\mathcal{F}_2$ from NC scattering as a function of x for fixed values of Q^2 as measured by ZEUS. Also shown are the data from the fixed target experiments BCDMS, E665, NMC and SLAC. The solid lines indicate the QCD NLO fit. Also shown are the MRSA', GRV94 and CTEQ3 parametrizations.

virtual photon is large compared to the interaction time, which means $x \ll 1/(2M_p \cdot R_p)$, where R_p is the proton radius, $R_p = 4$ GeV^{-1} [39]. This requirement is well satisfied if $x \ll 0.1$. The expression for $\mathcal{F}_2$ in terms of σ_{T} and σ_{L} is

$$\mathcal{F}_2(x,Q^2) = \frac{Q^2(1-x)}{4\pi^2\alpha}\sigma^{\mathrm{tot}}_{\gamma^* p}. \tag{19}$$

At small x the expression can be rewritten in terms of the virtual-photon proton c.m. energy W, $W^2 \approx Q^2/x$ leading to

$$\sigma^{\mathrm{tot}}_{\gamma^* p} \approx \frac{4\pi^2\alpha}{Q^2}\mathcal{F}_2(W, Q^2)\,. \tag{20}$$

Equation (20) was used by ZEUS [40] to determine from the 1993 $\mathcal{F}_2$ data $\sigma^{\mathrm{tot}}_{\gamma^* p}$. Figure 11 shows for the 1994 data $Q^2\sigma^{\mathrm{tot}}_{\gamma^* p}$ as a function of W from 20 to 260 GeV for fixed Q^2 between 15 and 70 GeV^2. The data cluster around a narrow band rising almost linearly with W. A fit of the form $Q^2\sigma^{\mathrm{tot}}_{\gamma^* p} = a + b \cdot W^{\varepsilon}$ gave the (preliminary) value of $\varepsilon \approx 0.9$ (a fit with a=0 yielded a smaller value, $\varepsilon_{a=0} \approx 0.5$, though with considerable larger χ^2/ndf). If $\sigma^{\mathrm{tot}}_{\gamma^* p}$ is described in terms of a pomeron trajectory, $\sigma^{\mathrm{tot}}_{\gamma^* p} \propto (W^2)^{\alpha_{I\!P}(0)-1}$ the intercept $\alpha_{I\!P}(0) = 1 + \frac{\varepsilon}{2} \approx 1.45$.

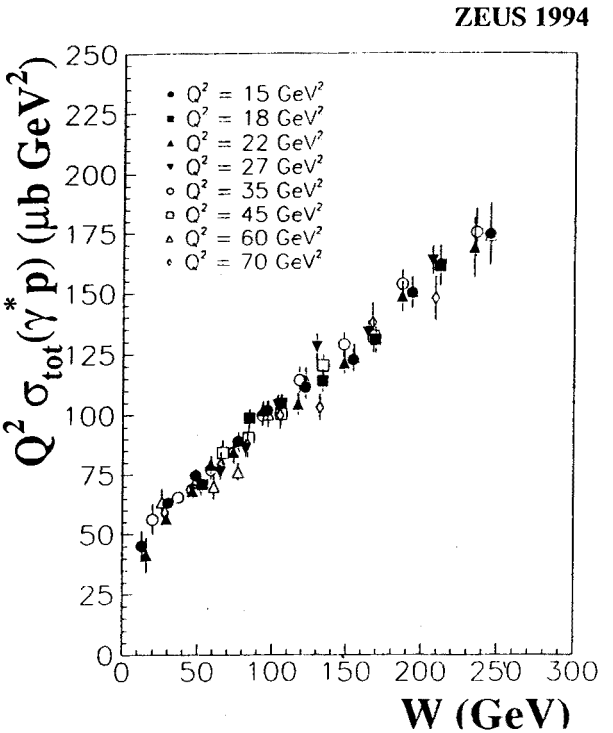

Fig. 11. $Q^2 \cdot \sigma^{\mathrm{tot}}_{\gamma^* p}$ as a function of W for fixed Q^2 between 15 and 70 GeV^2 as determined from the ZEUS data.

The observed rise of $\sigma^{\mathrm{tot}}_{\gamma^* p}$ is in marked contrast to the behaviour of the total cross section for antiproton–proton scattering and for *real* photon-proton scattering which are compatible with $\approx W^{0.2}$. Thus, the rise of

$\mathcal{F}_2$ as $x \to 0$ — or that of $\sigma^{\rm tot}_{\gamma^* p}$ as $W \to \infty$ - signals the presence of a new phenomenon. In QCD, the rise is the result of the strong increase of the number of partons at small x which fill the proton and reduce its transparency to high Q^2 photons.

2.7. Transition from photoproduction to DIS

ZEUS and H1 have made a special effort to study the structure function $\mathcal{F}_2$ in the transition region from photoproduction to deep inelastic scattering. Measurements have been performed for Q^2 values as low as 0.11 GeV^2 and x values as small as 10^{-6}. The data [9,41–43] are presented in Fig. 12 together with results from E665 [44] obtained at $x > 10^{-3}$. The steep increase of $\mathcal{F}_2$ as x tends to zero, observed at large Q^2 recedes smoothly as $Q^2 \to 0$.

A number of phenomenological models [45–50] have been put forward to describe the behaviour at low x and low Q^2. The curves in Fig. 12 show predictions of some of these models. The Vector Dominance type model DL [45] fails to reproduce the rise of $\mathcal{F}_2$ for Q^2 above ≈ 0.5 GeV^2. The BK model [47] assumes a VDM-like component which dominates the region of low Q^2 plus a hard QCD-like component for the high Q^2 regime. The predictions are somwhat above the data at low Q^2. The model CKMT [46] assumes at high Q^2 the dominance of a bare pomeron with an intercept of $\alpha_{I\!P}(0) \approx 1.24$. At low Q^2 the pomeron intercept is assumed to decrease due to rescattering corrections leading to $\alpha_{I\!P}(0) = 1.08$, the value obtained from hadron-hadron scattering. The CKMT predictions are found to be below the data for $Q^2 < 0.6 - 1$ GeV^2. The GRV model has been introduced above. It considers only the hard scattering contribution. The GRV predictions for $\mathcal{F}_2$ are close to zero for Q^2 near the evolution scale $Q^2 = 0.34$ GeV^2. At $Q^2 = 0.44$ GeV^2 GRV accounts for about 40% of the measured $\mathcal{F}_2$ and about 80% at $Q^2 = 0.57$ GeV^2. At $Q^2 = 0.9$ GeV^2 basically all of the DIS cross section is attributed to hard scattering. Taking the GRV result at face value, the transition from soft to hard scattering occurs at $Q^2 < 1$ GeV^2. The model ABY [49], which assumes a hard plus a soft component evolved in NLO-QCD, gives a rather good descripton of the full set of data.

3. NC and CC scattering at high Q^2

In the standard model, electron-proton scattering at low and medium Q^2 ($Q^2 \leq 1000$ GeV^2) proceeds almost exclusively through photon exchange. HERA offers the opportunity to reach much higher values of Q^2 where substantial contributions are expected also from the exchange of the heavy vector bosons $W^{\pm}$ and Z^0. The differential cross section for DIS is given in Eq. (8). In the following, the contributions from the longitudinal struc-

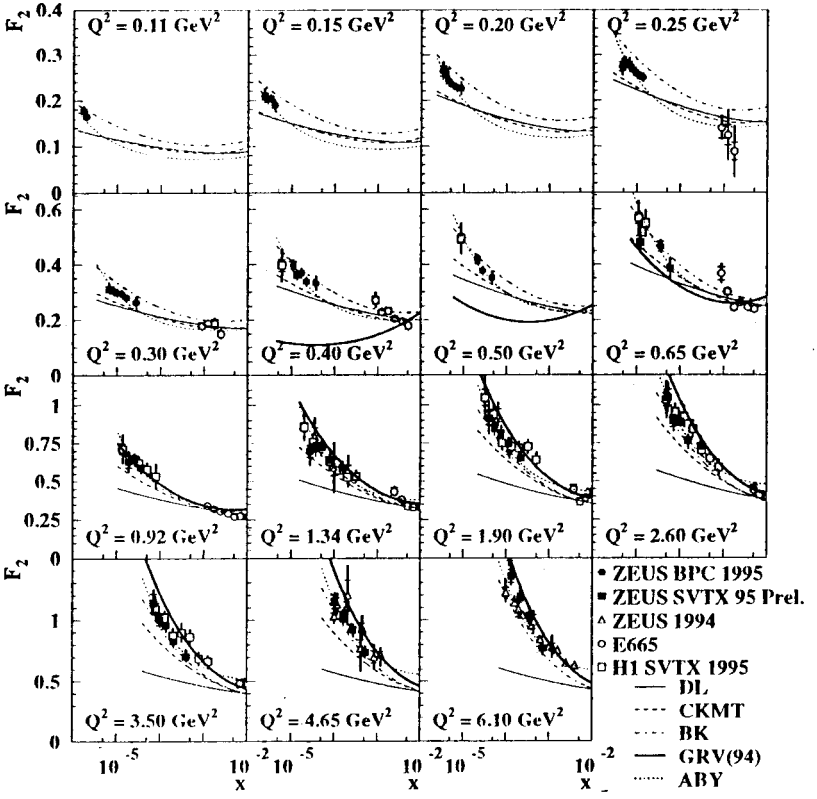

Fig. 12. F_2 as a function of x for constant Q^2 in units of GeV^2 as measured by ZEUS, H1 and E665. Also shown are the predictions of various models, see text.

ture functions, $\mathcal{F}_{\rm L}$, have been neglected. The structure functions can be expressed as sums over quark flavors of the proton's quark densities $q(x,Q^2)$ weighted according to the gauge structure of the scattering amplitudes. For the neutral current (NC) reaction, $e^{\pm}p \to e^{\pm}X$, mediated by γ and Z^0 exchange, they can be written as

$$\begin{aligned}\mathcal{F}_2^{\rm NC} &= x\sum_q [q(x,Q^2)+\overline{q}(x,Q^2)] \\ &\quad \times[e_q^2 e_e^2 - 2e_q v_q e_e v_e \chi_Z + (v_q^2+a_q^2)(v_e^2+a_e^2)\chi_Z^2], \qquad (21)\\ x\mathcal{F}_3^{\rm NC} &= x\sum_f [q(x,Q^2)-\overline{q}(x,Q^2)] \\ &\quad \times[-2e_q a_q a_e \chi_Z + 4v_q a_q v_e a_e \chi_Z^2], \qquad (22)\end{aligned}$$

where e_e is the electric charge of the incoming e in units of the elementary charge ($e_e = -1$ for electrons and $e_e = +1$ for positrons), a_e and v_e are the axial and vector couplings of the $e^{\mp}$ to the Z^o, and a_q and v_q are the analogous couplings for a quark of flavor q with the electric charge e_q. v_q and a_q are related to the third component of the weak isospin by $v_q = (T_{3q} - 2e_q \sin^2\theta_w)$ and $a_q = T_{3q}$. χ_Z is given by

$$\chi_Z = \frac{1}{4\sin^2\theta_w \cos^2_w} \frac{Q^2}{Q^2 + M_Z^2}, \tag{23}$$

where θ_w is the weak mixing angle and M_Z is the Z^0 mass.

For charged current (CC) reactions, $e^{\mp} p \to \nu_e(\overline{\nu}_e)X$, in which a W boson with mass M_W is exchanged, the functions are
for $e^- p$ scattering:

$$\mathcal{F}_2^{\mathrm{CC}} = \frac{x\mathcal{P}_W^2}{8sin^4\theta_W} \sum_{k,m} [|V_{km}|^2 u_k + |V_{mk}|^2 \overline{d}_m], \tag{24}$$

$$x\mathcal{F}_3^{\mathrm{CC}} = \frac{x\mathcal{P}_W^2}{8sin^4\theta_W} \sum_{k,m} [|V_{km}|^2 u_k - |V_{mk}|^2 \overline{d}_m], \tag{25}$$

and for $e^+ p$ scattering:

$$\mathcal{F}_2^{\mathrm{CC}} = \frac{x\mathcal{P}_W^2}{8\sin^4\theta_W} \sum_{k,m} [|V_{km}|^2 \overline{u}_k + |V_{mk}|^2 d_m], \tag{26}$$

$$x\mathcal{F}_3^{\mathrm{CC}} = \frac{x\mathcal{P}_W^2}{8\sin^4\theta_W} \sum_{k,m} [|V_{km}|^2 \overline{u}_k - |V_{mk}|^2 d_m], \tag{27}$$

where $k, m = 1, 2, 3$ are the generation indices of up-type quarks, $u_k(x, Q^2)$, and down-type antiquarks, $\overline{d}_m(x, Q^2)$, V is the Cabbibo–Kobayashi–Maskawa quark mixing matrix, θ_W is the weak mixing angle, and $\mathcal{P}_W = Q^2/(Q^2 + M_W^2)$. In lowest order of electroweak corrections, $G_F M_W^2 = \pi\alpha/\sqrt{2}\sin^2\theta_W$, where G_F is the Fermi constant.

In leading order QCD the CC cross sections simplify to

$$\frac{d^2\sigma_{e^- p\to\nu X}}{dx dQ^2} = \frac{G_F^2}{2\pi x} \frac{M_W^4}{(M_W^2 + Q^2)^2} \sum_{k=1}^{2} [u_k(x, Q^2) + (1-y)^2 \overline{d}_k(x, Q^2)], \tag{28}$$

$$\frac{d^2\sigma_{e^+ p\to\overline{\nu}X}}{dx dQ^2} = \frac{G_F^2}{2\pi x} \frac{M_W^4}{(M_W^2 + Q^2)^2} \sum_{k=1}^{2} [\overline{u}_k(x, Q^2) + (1-y)^2 d_k(x, Q^2)]. \tag{29}$$

Both the H1 [52] and ZEUS [54] experiments have previously reported cross section measurements, based on data collected in 1993, which established that the Q^2 dependence of the CC cross section is consistent with the expectations from the W propagator. The data from ZEUS established also that the CC and NC cross sections are of similar magnitude for $Q^2 \geq M_W^2$.

In Fig. 13 and Fig. 14 the differential cross sections $d\sigma/dQ^2$ as measured by H1 [53] and ZEUS [55,56] are shown for NC and CC $e^{\pm}p$ scattering using the 1993-1995 data. The ZEUS cross sections have been corrected to the Born level. The H1 cross sections are given for $p_T > 25$ GeV, where p_T is the transverse momentum of the hadronic system. This cut reduces the cross sections by about 30 % in the lowest Q^2 interval and by 10% or less at larger values of Q^2. The H1 data have not been corrected for radiative effects which increase (decrease) the measured cross sections by up to 19 (6) %.

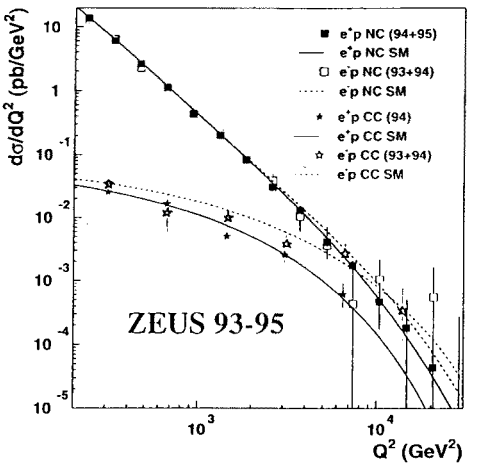

Fig. 13. Differential cross sections $d\sigma/dQ^2$ versus Q^2 for NC and CC e^-p and e^+p scattering as measured by ZEUS; preliminary values. The curves show the predictions of the standard model (SM).

The NC cross sections for e^-p and e^+p scattering exhibit a steep fall-off with Q^2 which is dominated by the photon propagator. The two cross sections are the same, within errors. The solid and dashed curves show the predictions of the standard model (SM). The differences between the two reactions arise from the $x\mathcal{F}_3$ term (see Eq. (8)). The precision of the data is not yet sufficient to establish the presence of this term.

The fall-off of the CC cross sections is less steep with Q^2. It reflects the effect of the W propagator, the decrease of the parton densities with increasing x and the $(1-y)^2$ terms in the cross sections. The differences between e^-p and e^+p scattering are small for $Q^2 < 4000$ GeV^2 as expected

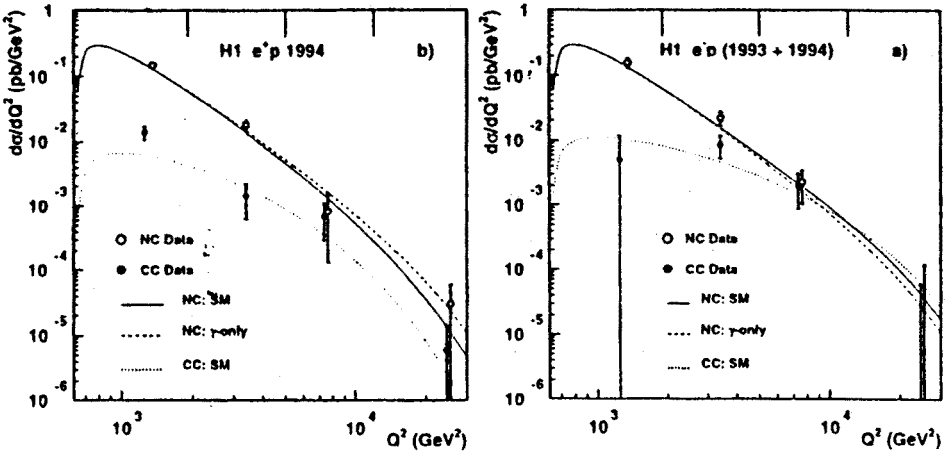

Fig. 14. Differential cross sections $d\sigma/dQ^2$ versus Q^2 for NC and CC e^-p and e^+p scattering as measured by H1; the data are not corrected for the cut $p_T > 25$ GeV, where p_T is the transverse momentum of the hadronic system, and for radiative effects. The curves show the predictions of the standard model (SM). For NC scattering the predictions for photon exchange only are also given.

for small x when the contribution from valence quarks can be neglected and $\bar{d}(x,Q^2) = \bar{u}(x,Q^2)$. At higher values of Q^2 the e^- cross sections is larger than the e^+p one. This is also expected since for e^+p the scattering on valence quarks is reduced by the $(1-y)^2$ factor and at large x the density of u-quarks is larger than that of d-quarks. The predictions of the SM are in agreement with the data.

For e^-p scattering and $Q^2 \geq 5000$ GeV^2 the CC cross section reaches about the same magnitude as the NC cross section: at these large values of Q^2 the weak force is of similar strength as the electromagnetic one. It is instructive to compare this result with typical electromagnetic and weak particle decays where the weak force is about ten orders of magnitude smaller than the electromagnetic one. For instance, the decay time for the electromagnetic decay $\Sigma^0 \to \Lambda\gamma$ is $7.4 \pm 0.7 \cdot 10^{-20}$ s while it is $4.1 \cdot 10^{-10}$ s for the weak decay $\Lambda \to p\pi^-$ [57](note, both decays have similar c.m. momentum, viz. 0.10 GeV and 0.074 GeV, respectively, and therefore similar phase space).

The measured CC cross sections are inconsistent with the expectations for an infinite propagator mass. Fits where M_W was treated as a free pa-

rameter yielded

$$M_W = 84^{+9\ +5}_{-6\ -4}\text{GeV (H1)},$$
$$M_W = 79^{+8\ +4}_{-7\ -4}\text{GeV (ZEUS)}.$$

The combined H1 and ZEUS result is

$$M_W = 82^{+6\ +3}_{-5\ -3}\text{GeV}.$$

These values are in good agreement with M_W measured directly, $M_W = 80.410 \pm 0.090$ GeV [68].

4. Deep inelastic scattering at high-Q^2, high-x

The results on structure functions presented in Section 2 have been obtained in NC scattering at Q^2 values below 5000 GeV^2 in a kinematical region which is dominated by photon-exchange. As one climbs up to Q^2 values of the order of M_W^2, M_Z^2, contributions from vector-boson exchange become important as evidenced by the data shown in the previous section. During 1994-96 H1 and ZEUS have collected for the first time sufficient data for a first look at deep inelastic e^+p scattering beyond Q^2 values of 10 000 GeV^2. As Q^2 increases finer and finer details in the proton (electron) can be resolved: for $Q^2 > 10000$ GeV^2 objects smaller than $2 \cdot 10^{-16}$, corresponding to a fraction of 10^{-3} of the proton diameter, can be resolved. In this regime, lepton-nucleon scattering allows unique and sensitive tests of the Standard Model (SM) as well as of certain extensions of it [58].

First results for the high Q^2 regime have been presented by H1 and ZEUS in [59,60] from data obtained in 1994-1996 for integrated luminosities of 14 and 20 pb^{-1}, respectively. Thanks to the excellent performance of HERA, the data taken during the first part of the 1997 running period have increased the data samples by a factor of about 1.7. The preliminary results from these data have been combined with those from 1994-1996 and have been presented by [61,62]. They will be discussed in the following.

4.1. Reconstruction of the event kinematics

Due to the near-hermeticity of the H1 and ZEUS detectors, the Lorentz-invariant variables x (or y) and Q^2 characterizing a deep inelastic scattering (see Fig. 15) can be determined from the energy E'_e and scattering angle θ'_e of the scattered positron or from the energy $\sum_h E_h$ and average production angle γ_h of the hadron system or from a combination of these quantities provided the incoming positron did not radiate.

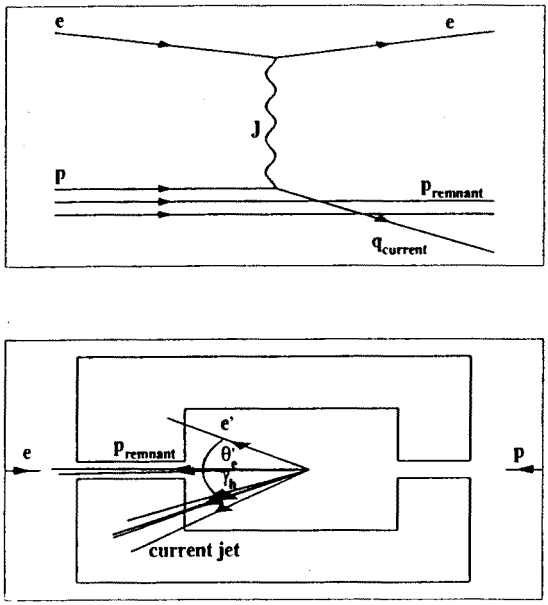

Fig. 15. DIS, $ep \to eX$, without ISR: diagram (top) and event configuration in a HERA detector (bottom).

The electron side yields:

$$y = 1 - \frac{E'_e}{2E_e}(1 - \cos\theta'_e)\,,$$

$$Q^2 = 2E_e E'_e(1 + \cos\theta'_e)\,,$$

$$x = E'_e \frac{1 + \cos\theta'_e}{2yE_p}\,, \tag{30}$$

where E_e, E_p are the beam energies and the angles are measured wrt. the proton beam direction. Using the method of Jacquet–Blondel [63] the hadron variables can be determined approximately by summing the energies (E_h) and transverse (p_{Th}) and longitudinal momenta (p_{Zh}) of all final state particles. The method rests on the assumption that the total transverse momentum carried by those hadrons which escape detection through the beam hole in the proton direction as well as the energy carried by particles escaping through the beam hole in the electron direction can be neglected. The result is:

$$
\begin{aligned}
y_{\mathrm{JB}} &= \frac{1}{2E_e}\sum_h (E_h - p_{Zh}), \\
Q^2_{\mathrm{JB}} &= \frac{(\sum_h p_{Xh})^2 + (\sum_h p_{Yh})^2}{1 - y_{\mathrm{JB}}} \\
x_{\mathrm{JB}} &= Q^2_{\mathrm{JB}}/(y_{\mathrm{JB}} s).
\end{aligned} \tag{31}
$$

In CC scattering, where the outgoing lepton is a neutrino and escapes undetected, the event kinematics is reconstructed with the JB method.

The double-angle (DA) method of [64] uses the electron scattering angle and the angle γ_h which characterizes the longitudinal and transverse momentum flow of the hadronic system (in the naive quark-parton model γ_h is the scattering angle of the struck quark):

$$
\cos\gamma_h = \frac{(\sum_h p_{Xh})^2 + (\sum_h p_{Yh})^2 - (\sum_h (E_h - p_{Zh}))^2}{(\sum_h p_{Xh})^2 + (\sum_h p_{Yh})^2 + (\sum_h (E_h - p_{Zh}))^2} \tag{32}
$$

leading to

$$
\begin{aligned}
Q^2_{\mathrm{DA}} &= \frac{4E_e^2 \sin\gamma_h (1 + \cos\theta'_e)}{\sin\gamma_h + \sin\theta'_e - \sin(\gamma_h + \theta'_e)}, \\
x_{\mathrm{DA}} &= \frac{E_e}{E_p} \frac{\sin\gamma_h + \sin\theta'_e + \sin(\gamma_h + \theta'_e)}{\sin\gamma_h + \sin\theta'_e - \sin(\gamma_h + \theta'_e)}, \\
y_{\mathrm{DA}} &= \frac{\sin\gamma_h (1 + \cos\theta'_e)}{\sin\gamma_h + \sin\theta'_e + \sin(\gamma_h + \theta'_e)}, \\
&= \frac{(1 - \cos\gamma_h)\sin\theta'_e}{\sin\gamma_h + \sin\theta'_e - \sin(\gamma_h + \theta'_e)}, \\
&= \frac{Q^2_{\mathrm{DA}}}{x_{\mathrm{DA}} s}.
\end{aligned} \tag{33}
$$

The DA method is insensitive to the energy scales for the measurement of the final state particles.

H1 used the electron variables (x_e, y_e, Q^2_e) as the principal method of reconstruction and the DA variables $(x_{\mathrm{DA}}, y_{\mathrm{DA}}, Q^2_{\mathrm{DA}})$ for a cross check while ZEUS made the opposite choice.

As mentioned before, in deriving these relations it was assumed that the incoming e does not radiate. The energy carried away by initial state radiation, E_{ISR}, can be limited by considering the quantity δ which measures the difference of the energies and longitudinal momenta summed over all particles observed in an event:

$$
\delta = \sum_h (E_h - p_{Zh}) + E'_e(1 - \cos\theta'). \tag{34}
$$

For a hermetic detector, $\delta = 2E_e$; if the ISR photon escapes detection,

$$E_{ISR} = E_e - \delta/2\,. \tag{35}$$

For ep collisions where the incoming e fuses with a quark of the proton to form a resonant state (*e.g.* a leptoquark LQ as depicted in Fig. 16) decaying into an e and a hadron system, the mass M of this state is given by

$$M^2 = xs\,, \tag{36}$$

provided initial state radiation and the mass of the hadronic system can be neglected.

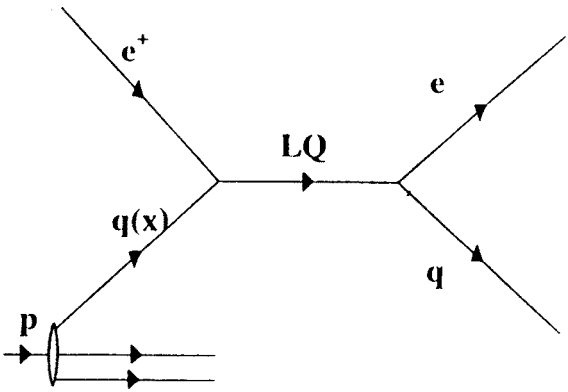

Fig. 16. Diagram for leptoquark production by ep scattering.

The resolutions for x, y, Q^2 expected by H1 and ZEUS for the high Q^2 regime are summarized in Table IV.
The accuracy with which the event kinematics in the $y - M$ plane can be reconstructed by the different methods is illustrated in Fig. 17 for the H1 experiment. The e and DA methods provide a rather precise determination of y over almost the full phase space; the resolution in M (or equivalently in x) improves as y increases. The JB method is inferior to the e and DA methods; for CC events the reconstruction of the event kinematics becomes difficult at large y.

TABLE IV

Resolution of kinematic parameters

H1	ZEUS
	$\delta\theta_e = 0.3°$ $\delta\gamma_h = 1.7°$ at small γ_h $\delta\gamma_h = 2.9°$ at $\gamma_h = 90°$
$y_e > 0.1$: $\frac{\delta x_e}{x_e} = 2\frac{\delta M_e}{M_e}$ $\delta M_e = 7$ GeV	$x > 0.2$: $y = 0.2 - 0.55$: $\frac{\delta x_{\rm DA}}{x_{\rm DA}} \approx 0.085$ $y = 0.55 - 0.9$: $\frac{\delta x_{\rm DA}}{x_{\rm DA}} \approx 0.05$
$187.5 < M_e < 212.5$GeV, $y_e > 0.4$: $\delta x_e = 0.022$ $\delta y_e = 0.015$ $\frac{\delta Q^2_e}{Q^2_e} = 0.027$ $\delta M_e = 5$ GeV	$x_{\rm DA} > 0.55, y_{\rm DA} > 0.25$: $\delta x_{\rm DA} = 0.041$ $\delta y_{\rm DA} = 0.012$ $\frac{\delta Q^2_{\rm DA}}{Q^2_{\rm DA}} = 0.038$ $\delta M_{\rm DA} = 9$ GeV

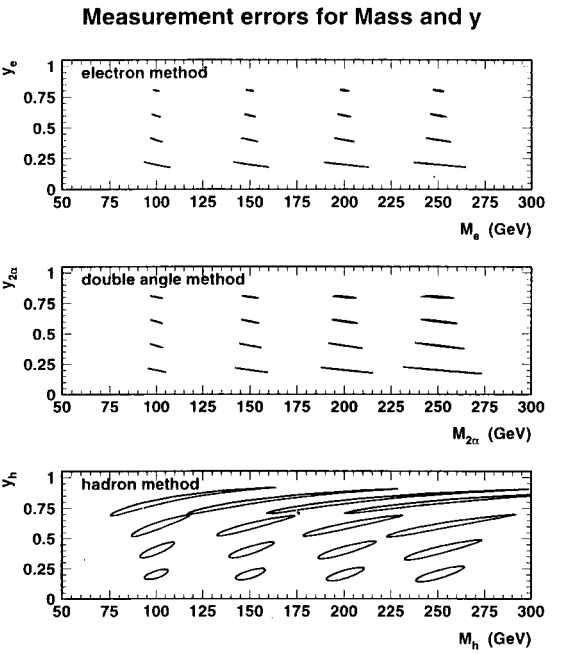

Fig. 17. Expected uncertainties in the reconstruction of the event kinematics in terms of (y, M) for the H1 experiment using the e, DA and JB methods. Shown are one standard deviation error ellipses.

4.2. Neutral current scattering

4.2.1. Event selection

The main criteria employed by the two experiments for selecting DIS-NC events at large Q^2 are listed in Table V.

TABLE V

Parameters, selection criteria and efficiencies for the DIS NC high Q^2 analyses

parameter	H1		ZEUS	
int. lumi.	23.7pb^{-1}	effic. %	34.3pb^{-1}	effic. %
longt. vtx	$\lvert Z_v - Z_0\rvert < 35$cm		$\lvert Z_v\rvert < 50$cm	94.9
δ	$43 < \delta < 63$GeV	≈ 90	$40 < \delta < 70$GeV	92.0
e	$p_{T,e} < 25$GeV	> 90	$E_e > 20$ GeV	89.4
e isolat.				87.2
θ_e	$> 10°$		$\theta > 0.3$:	
			track+clust	85.7
			$\theta < 0.3$:	
			$p_{Te} > 30$GeV	83.9
			$\theta < 0.3$:	
			$\delta > 44$GeV	83.8
			rej when 2 em cl	83.4
$p_{T\text{miss}}/\sqrt{p_{Te}}$	$3\ \text{GeV}^{0.5}$			
tot. effic. (%)		≈ 80	$Q^2_{\text{DA}} > 5000\ \text{GeV}^2$	81.5
	n. events		n. events	
$0.1 < y < 0.9$				
$Q^2 > 2500\text{GeV}^2$	724			
$Q^2 > 5000\text{GeV}^2$	193		326	

4.2.2. Prediction of the Standard Model for NC scattering

The reaction studied is

$$e^+ p \to e + X\,, \tag{37}$$

where X represents the final state hadronic system. In the high Q^2 regime, the SM neutral current cross section depends on the (well-measured) electroweak parameters and on the parton densities in the proton. Though the latter have not been measured in the high Q^2 region under study, perturbative QCD (pQCD) predicts their values through evolution from high-precision measurements made at lower Q^2 values [66].

The Born cross section for the NC DIS reaction Eq. (37) with unpolarized beams is given by Eq. (8) with the structure functions as expressed [1] in Eq. (21), (22). In the region of large x and large Q^2 the parity-violating $x\mathcal{F}_3$ term substantially reduces (increases) the cross section for e^+p (e^-p) scattering.

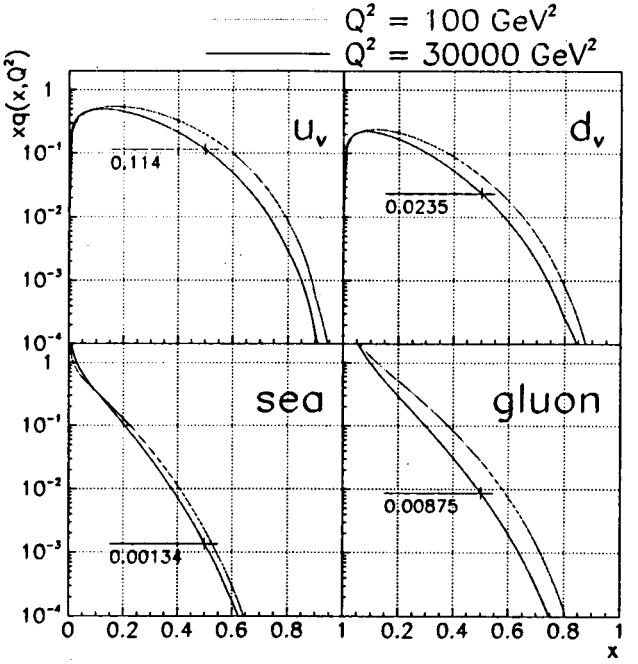

Fig. 18. The parton momentum densities xu_v, xd_v, xq_{sea}, xg in the proton as a function of x for $Q^2 = 100$ and 30000 GeV^2.

All electroweak parameters relevant for this study have been measured with high precision [57,68]. The QCD evolved structure functions of Eq. (22), evaluated at a given x and high Q^2, depend on quark and gluon densities in the proton measured at lower Q^2 for the same and higher values of x. For the parton densities H1 used the MRS-H set of [69], ZEUS those of [70]; the latter are shown in Fig. 18 as a function of x for Q^2 values of 100 (lower curve) and 30 000 GeV^2 (upper curve) taken from [61]. At high x, u quarks give the dominant contribution to the cross section because they have the largest density [71] and because their electric charge is large, $e_u = \frac{2}{3}$. The

[1] The contribution to the cross section Eq. (8) from the longitudinal structure function $\mathcal{F}_L$ was estimated with pQCD using the parton densities of [67] to be less than 1% in the kinematic region under study [60].

antiquark ($\bar{q}$) density is small [72]: *e.g.* at $Q^2 = 30\,000$ GeV^2 the density of sea quarks is two orders of magnitude below that of the valence quark u_v. For $x = 0.5$ more than 90% of the cross section results from production on the u_v.

The reduced cross section,

$$\tilde{\sigma}(e^+p) = \frac{xQ^4}{2\pi\alpha^2}\frac{1}{1+(1-y)^2}\frac{d^2\sigma}{dxdQ^2} = \mathcal{F}_2 - \frac{1-(1-y)^2}{1+(1-y)^2}x\mathcal{F}_3, \quad (38)$$

is shown in Fig. 19 as a function of Q^2 for fixed values of x together with the data points from BCDMS, NMC and SLAC, which have been used in calculating the MRS-H set and which reach Q^2 values up to 250 GeV^2. The fall-off above $Q^2 \approx M_Z^2$ is due to the negative contribution from the $x\mathcal{F}_3$ term. Also given in Fig. 19 are the published data from ZEUS [9] and preliminary results from H1 [62] which cover Q^2 values up to 5000 GeV^2 and x values up to 0.55; they had not been used in extracting the MRS-H set. The HERA data are found to be well described by the evolution of the MRS-H set.

The uncertainties of the predictions for the Born-level e^+p DIS cross section in the region of high x and high Q^2 are estimated to be 6.5%, mainly due to uncertainties in the evolved quark densities.

The number of events predicted by SM were computed by Monte Carlo methods including electroweak corrections using the HERACLES program [73]. The code takes all box graphes into account, in particular the exchanges [2] of two γ's, of $\gamma - Z^0$ and $Z^0 - Z^0$. Also included in the simulation were the detector effects.

The theoretical and experimental uncertainties in the predicted number of SM events are summarized below [61]:

theoretical:	
electroweak parameters	0.25%
radiative corrections	2.0%
structure functions (dominated by uncertainties in the fixed target data)	6.5%
experimental:	
energy scales, smearing, resolutions	
– H1 (lowest to highest Q^2)	8.5 – 30%
– ZEUS ($x > 0.55, y > 0.25$)	8.5%

The overall uncertainties in the SM expectations are less than 35%.

[2] The program HECTOR [74] was used to check the cross sections computed using HERACLES. The differences were found to be about 1.5% of the integrated cross sections at $x_{DA} > 0.5, y_{DA} > 0.25$, see [60].

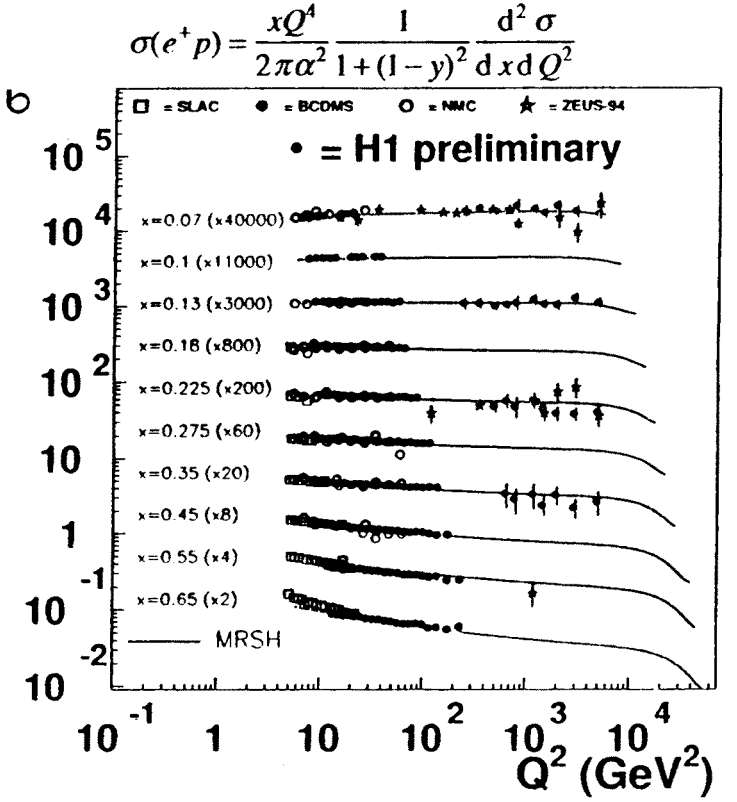

Fig. 19. The reduced cross section, $\tilde{\sigma}(e^+p)$ for fixed x as a function of Q^2. The data shown from BCDMS, NMC and SLAC have been included in determining the MRS-H parametrization (curves). Also shown are data from H1 (preliminary) and ZEUS; they had not been included in the MRS-H analysis.

4.2.3. Contamination from background processes

Potential backgrounds to the e^+p DIS events at large x and large Q^2 are those processes which yield an isolated positron or electron of high transverse momentum, or a photon or π^0 which could be identified as a scattered positron. The most serious candidate processes were found to be photoproduction of jets with large transverse energy, production of prompt photons, two-photon processes and production and decay of W, Z^o. However, both experiments found that the number of background events at high x, high Q^2 expected in their 1994-97 data sample is negligible (H1: < 0.1 event for $Q^2 > 10000\text{GeV}^2$, ZEUS: < 0.1 event for $x > 0.45, y > 0.25$).

4.2.4. Experimental results and comparison with the SM

In the following the results obtained by H1 and ZEUS for $ep \to eX$ are presented and compared with the expectations from the SM. The H1 results were obtained with the electron method, those of ZEUS with the DA method.

H1 results:

Figure 20(top) shows the number of events as a function of Q_e^2. The number of events observed ($N_{\rm obs}$, dots) agree well with the SM predictions ($N_{\rm pred}$, histogram) for Q_e^2 up to about 15000 GeV^2 while at higher Q_e^2 the data exceed the expectations by a factor of 2–5 seen also in the bottom of Fig. 20, where the ratio of observed to expected number of events is given.

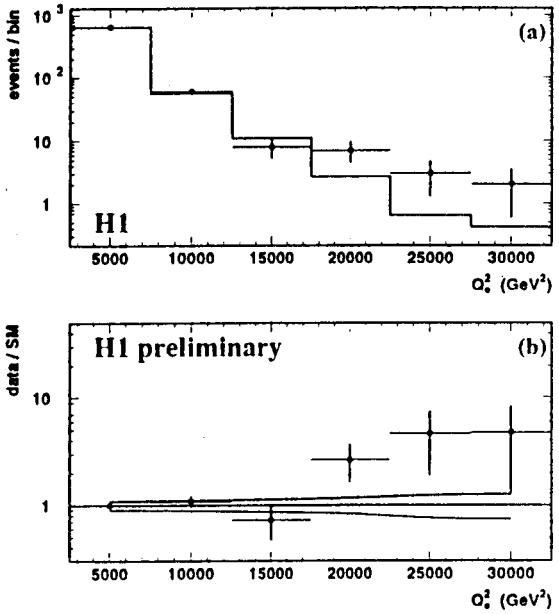

Fig. 20. Process $e^+p \to eX$, results from H1: (top) Q_e^2 distribution of number of events observed (dots) and predicted by the SM (histogram), (bottom) Ratio of observed and expected number of events as a function of Q_e^2. The lines above and below unity specify $\pm$ 1 s.d. limits for the SM prediction.

The comparison between observed and predicted number of events yields for $Q_e^2 > Q_{e,\rm min}^2$:

$Q^2_{\rm min}$(GeV^2)	$N_{\rm obs}(Q_e^2 > Q^2_{\rm min})$	$N_{\rm pred}(Q_e^2 > Q^2_{\rm min})$	$\mathcal{P}$
2500	724	714 ± 69	36%
15000	18	8.00 ± 1.16	0.34%.

Here $\mathcal{P}$ is the probability [3], that $\geq N_{\rm obs}$ events are observed when $N_{\rm pred}$ events are predicted, $\mathcal{P} = \sum_{n=N_{\rm obs}}^{\infty} \frac{\mu^n}{n!} e^{-\mu}$ where $\mu = N_{\rm pred}$.

Figure 21(top) shows the number of events as a function of M_e for $y_e > 0.4$. The numbers of events observed ($N_{\rm obs}$, dots) agree well with the SM predictions ($N_{\rm pred}$, histogram) for M_e up to about 175 GeV while in the mass bin 187.5–212.5 GeV the data exceed the expectations by a factor of about 5, (see bottom of Fig. 21).

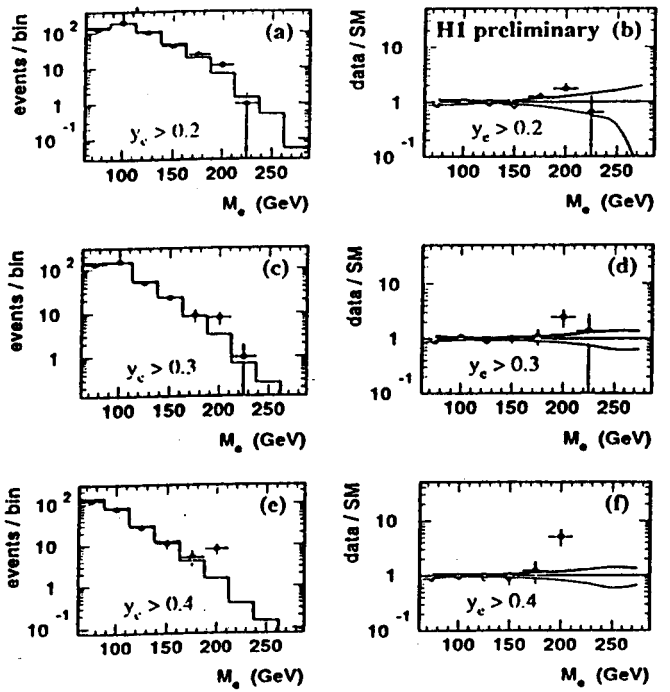

Fig. 21. Process $e^+p \to eX$, results from H1 for $y_e > 0.4$: (left) M_e distribution of number of events observed (dots) and predicted by the SM (histogram). (right) Ratio of observed and expected number of events as a function of M_e. The lines above and below unity specify $\pm$ 1 s.d. limits for the SM prediction.

The comparison between observed and predicted number of events yields for $187.5 < M_e < 212.5$ GeV the following result:

$N_{\rm obs}$	$N_{\rm pred}$	$\mathcal{P}$
8	1.53 ± 0.29	0.033%

The probability to see an excess with this significance in *some* window of M is about 1%.

[3] using the central value

The distribution of y_e versus M_e is displayed in Fig. 22. The excess of events over the SM predictions is found to occur in the region of $Q^2 > 15000$ GeV^2 *and* masses around 200 GeV.

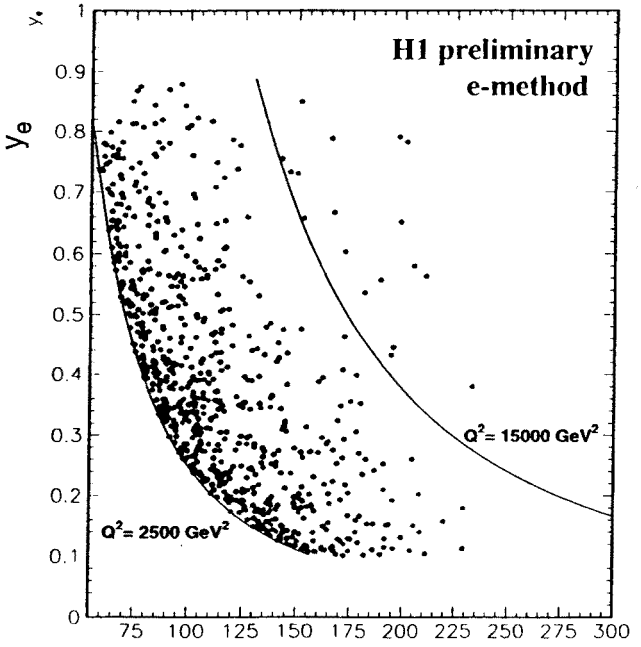

Fig. 22. Process $e^+p \to eX$, results from H1: distribution of y_e versus M_e.

ZEUS results:

Figure 23(top) shows the number of events as a function of $Q^2_{\rm DA}$. The number of events observed ($N_{\rm obs}$, dots) agree well with the SM predictions ($N_{\rm pred}$, histogram) for $Q^2_{\rm DA}$ up to about 20000 GeV^2 as seen also from the bottom plot which compares the cumulative Q^2 distributions observed and expected.

The comparison between observed and predicted number of events yields for $Q^2_{\rm DA} > Q^2_{\rm min}$:

$Q^2_{\rm min}$(GeV^2)	$N_{\rm obs}(Q^2_{\rm DA} > Q^2_{\rm min})$	$N_{\rm pred}(Q^2_{\rm DA} > Q^2_{\rm min})$	$\mathcal{P}$
5000	326	328 ± 15	55%
35000	2	0.242 ± 0.017	2.5%.

Figure 24(top) shows the number of events as a function of $x_{\rm DA}$ for $y_{\rm DA} > 0.25$. The number of events observed ($N_{\rm obs}$, dots) agree well with the SM

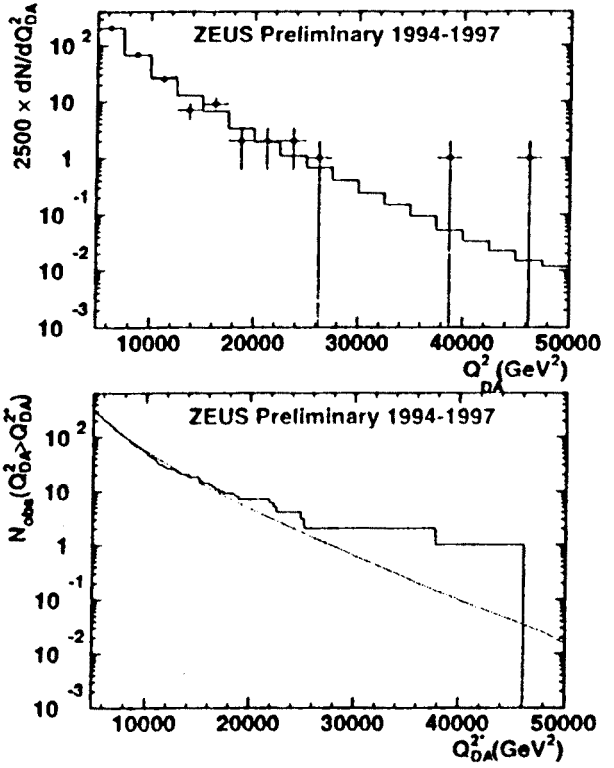

Fig. 23. Process $e^+p \to eX$, results from ZEUS: (top) $Q^2_{\rm DA}$ distribution of number of events observed (dots) and predicted by the SM (histogram). (bottom) The histogram indicates the number of events observed with $Q^2_{\rm DA} > Q^{2*}_{\rm DA}$ as a function of $Q^{2*}_{\rm DA}$. The dotted line shows the number of events expected by the SM.

predictions ($N_{\rm pred}$, histogram) for $x_{\rm DA}$ up to about 0.5 while there is an excess at higher $x_{\rm DA}$ values, see also bottom of Fig. 24.

The comparison between observed and predicted number of events yields for $x_{\rm DA} > 0.55, y_{\rm DA} > 0.25$:

$N_{\rm obs}$	$N_{\rm pred}$	$\mathcal{P}$
5	1.51 ± 0.13	1.9%

The distribution of $y_{\rm DA}$ versus $x_{\rm DA}$ is displayed in Fig. 25. The excess of events over the SM predictions is observed at $Q^2 > 15000$ GeV^2 *and* $x_{\rm DA}$ around 0.6.

Combined H1 and ZEUS results:

The H1 and ZEUS cross sections integrated over Q^2: $\sigma(Q^2 > Q^2_{\rm min})$, and corrected for detector and radiative effects are compared with the predicted

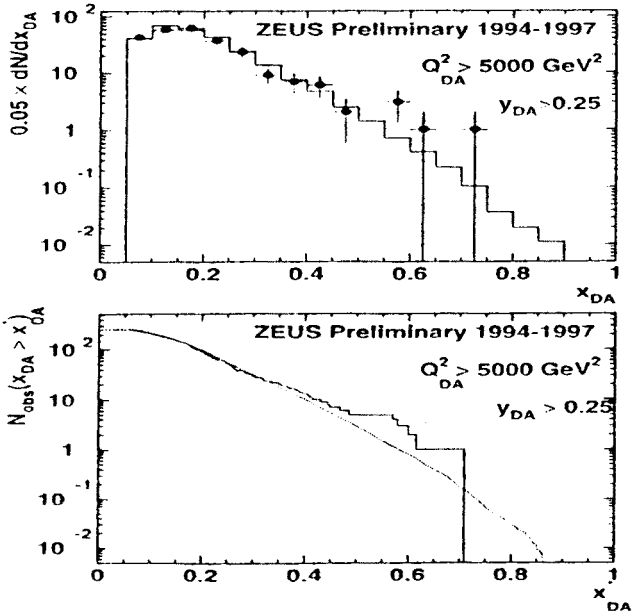

Fig. 24. Process $e^+p \to eX$, results from ZEUS for $y_{\mathrm{DA}} > 0.25$: (top) x_{DA} distribution of number of events observed (dots) and predicted by the SM (histogram). (bottom) The histogram indicates the number of events observed with $x_{\mathrm{DA}} > x^*_{\mathrm{DA}}$ as a function of x^*_{DA}. The dotted line indicates the number of events expected by the SM.

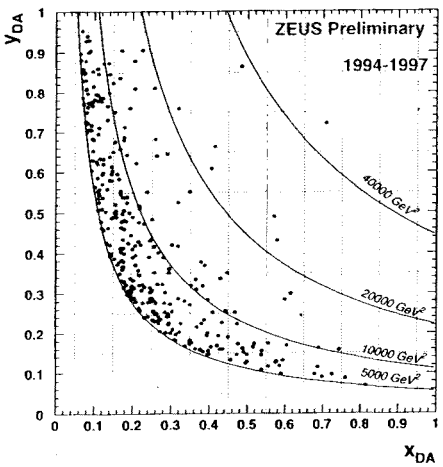

Fig. 25. Process $e^+p \to eX$, results from ZEUS: distribution of y_{DA} versus x_{DA}.

ones and are tabulated in Table VI and plotted in Fig. 26. There is good agreement between the two experiments; both show an excess over the SM predictions for $Q^2 > 20000$ GeV^2. The likelihood probability that the real cross section is below the SM prediction — *i.e.*, the probability that there is no excess — is 1.2% for $Q^2 > 20000$ GeV^2 and 0.24% for $Q^2 > 30000$ GeV^2.

TABLE VI

Reaction $e^+p \to eX$: preliminary cross sections for $Q^2 > Q^2_{\min}$ from H1 and ZEUS, [61].

$Q^2_{\min}$	H1		ZEUS		H1+ZEUS	
[GeV^2]	N_{obs}	σ [pb]	N_{obs}	σ [pb]	σ_{comb} [pb]	σ_{SM} [pb]
2500	724	$43.3^{+4.6}_{-3.9}$				
5000	193	$10.3^{+1.4}_{-1.2}$	326	$10.9^{+0.8}_{-0.8}$	$10.7^{+0.7}_{-0.7}$	10.6
10000	31	$1.66^{+0.42}_{-0.33}$	50	$1.73^{+0.28}_{-0.25}$	$1.70^{+0.23}_{-0.20}$	1.79
15000	18	$0.93^{+0.32}_{-0.24}$	18	$0.60^{+0.16}_{-0.14}$	$0.71^{+0.14}_{-0.12}$	0.49
20000	7	$0.42^{+0.21}_{-0.15}$	7	$0.24^{+0.11}_{-0.08}$	$0.30^{+0.092}_{-0.076}$	0.161
25000	4	$0.28^{+0.19}_{-0.12}$	3	$0.10^{+0.07}_{-0.05}$	$0.16^{+0.069}_{-0.053}$	0.059
30000	2	$0.21^{+0.24}_{-0.12}$	2	$0.067^{+0.060}_{-0.037}$	$0.098^{+0.059}_{-0.042}$	0.023
35000			2	$0.060^{+0.059}_{-0.037}$		0.0091
40000			1	$0.032^{+0.044}_{-0.023}$		0.0036

In Fig. 27 the distributions of y versus M are shown from H1 (reconstructed with the e-method) and ZEUS (reconstructed with the DA-method). Also indicated are the signal regions chosen by the two experiments. The two signal regions are disjunct in the mass M.

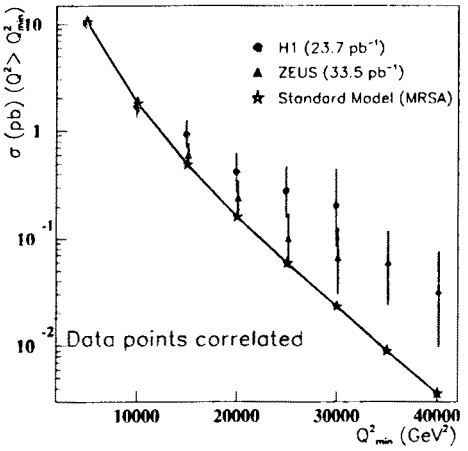

Fig. 26. Reaction $e^+p \to eX$: Preliminary cross sections for $Q^2 > Q^2_{\min}$ as a function of $Q^2_{\min}$ from H1 and ZEUS, [61].

The number of events observed by the two experiments in the two signal regions are as follows:

signal region	H1(e)	ZEUS(DA)
$187.5 < M < 212.5$ GeV	$N_{\text{obs}} = 8$	$N_{\text{obs}} = 3$
and $y > 0.4$	$N_{\text{pred}} = 1.53 \pm 0.29$	$N_{\text{pred}} = 2.94 \pm 0.24$
$x > 0.55$	$N_{\text{obs}} = 1$	$N_{\text{obs}} = 5$
and $y > 0.25$	$N_{\text{pred}} = 0.752 \pm 0.305$	$N_{\text{pred}} = 1.51 \pm 0.13$

In the signal region of H1, where H1 sees an excess of events, the number of events observed by ZEUS is consistent with the expectation from the SM, and vice versa.

At first glance, the results of the two experiments seem to be incompatible with the production of a single narrow resonance (*e.g.* a leptoquark LQ) with a mass M around 200–230 GeV. It is important to notice, however, that the two experiments used different methods for reconstructing the event kinematics, namely H1 used the e-method and ZEUS the DA-method.

The mass of a leptoquark M reconstructed with these methods via $M^2 = xs$ is incorrect in the presence of initial state radiation (ISR) [75,76], gluon radiation from the decay quark, hadronisation of the quark(+gluon) system from LQ decay and/or hadronisation of the proton remnant (see Fig. 28). The influence of these effects on the determination of M by the e and DA-methods was studied by generating events of the type

$$ep \to e' + \gamma_{\text{ISR}} + p \to LQ + \gamma_{ISR} + p_{\text{remnant}}$$

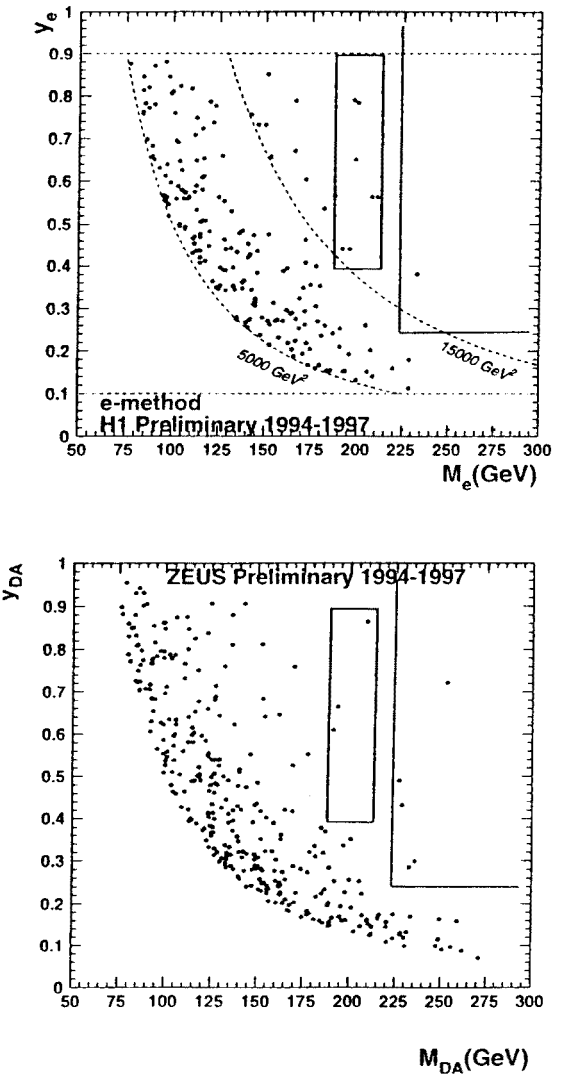

Fig. 27. Process $e^+p \to eX$, results from H1 (top) and ZEUS (bottom): distribution of y versus M determined with the e-method by H1 and with the DA-method by ZEUS. The boxes of smaller (larger) masses correspond to the H1 (ZEUS) signal regions.

$$\to (e'' + \text{had}) + \gamma_{ISR} + p_{\text{remnant}}. \tag{39}$$

and considering the 4-momenta of the final state particles. Detector effects were not taken into account.

The LQ was assumed to have $M = 200$ GeV and to be a scalar, decaying

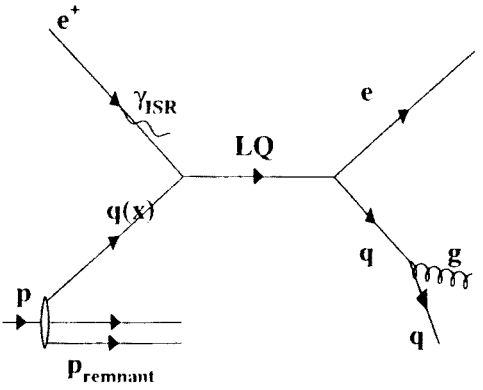

Fig. 28. Diagram for leptoquark production by ep scattering in the presence of initial state radiation and gluon emission.

uniformly in y. One of the three effects: ISR, massive hadron system, massive proton remnant, was turned on at a time, and the average mass $\overline{M}$ was determined with the e and DA-methods. The mass of the system $e'' +$ had is always 200 GeV, of course. The resulting mass distributions are shown in Fig. 29 yielding the following average mass values where $f_\gamma = E_{\rm ISR}/E_{\rm ebeam}$:

	$\overline{M_e}$	$\overline{M_{\rm DA}}$
$f_\gamma = 0.1$	196 GeV	222 GeV
$M_{\rm had} = 40$ GeV	190 GeV	190 GeV
$M_{p-\rm remnant} = 20$ GeV	199 GeV	200 GeV

ISR and a massive hadron system from LQ decay can produce large shifts of the reconstructed M value while a massive proton remnant has only a small effect. The shift of M_e by ISR depends on y: M_e is less (larger) than M for y less (greater) than $0.5 - (f_\gamma/4)/(1 - f_\gamma/2) \approx 0.5$ if $f_\gamma < 0.1$. H1 applies a cut $y > 0.4$ making the ISR effect modest. In contrast, ISR can produce large positive shifts of the mass determined by the DA-method, $M_{\rm DA} = M/1 - f_\gamma$ [4]. A massive hadron system from LQ decay shifts M_e and $M_{\rm DA}$ to lower values.

The data presented by H1 and ZEUS have been corrected, on average, for ISR. For small event samples, such as those discussed here, ISR as well as massive hadron systems, can have large effects on individual events [5].

[4] ISR will also shift $Q^2_{\rm DA}$ to higher values, $Q^2_{\rm DA} = \frac{Q^2}{(1-f_\gamma)^2}$ while y remains unchanged, $y = y_{\rm DA}$.

[5] From the comparison of the e and DA variables 1–2 events in each of the two experiments are likely to have ISR with $f_\gamma \approx 0.1$, see also [76, 77].

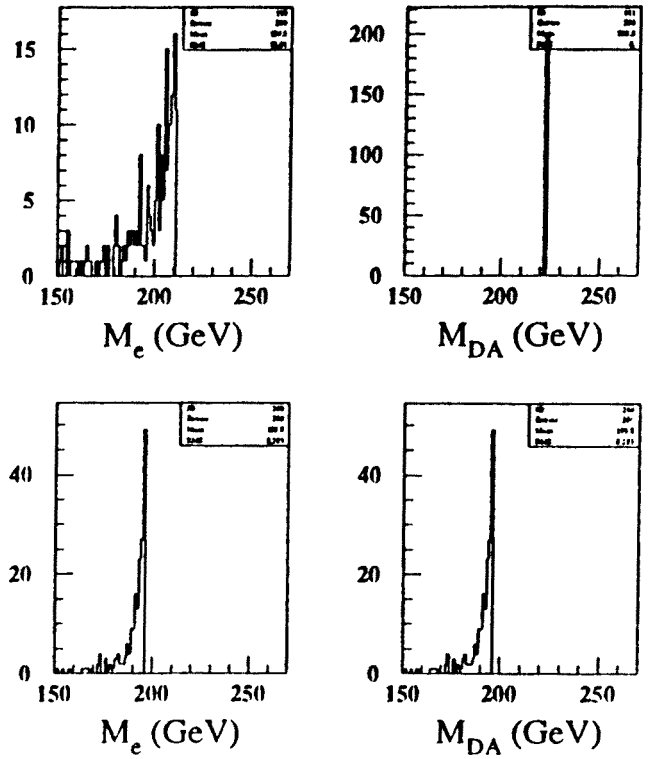

Fig. 29. Distributions of the mass M reconstructed with the e and DA methods, respectively, for the case of ISR with $f_\gamma = 0.1$ and $M_{\rm had} = 0$ (top) and no ISR but $M_{\rm had} = 40$ GeV (bottom).

Clearly, it is best to determine M directly from the 4-momenta of the $(e + \text{had})$ system, a procedure which does not suffer from ISR nor from the massiveness of the hadronic system. H1 has presented $(e + \text{jet})$ mass values for the events in the signal region from the 1994-96 sample [59]. Here, the jet with the highest transverse energy has been taken which may lead to an underestimate of $M_{e+\rm had}$. The uncertainties of 3–4% in the energy scales can introduce a systematic uncertainty on $M_{e+\rm jet}$ of similar magnitude, $\Delta M_{e+\rm jet} \approx 7$ GeV.

The masses obtained by H1 and ZEUS from an average over the events in the signal regions are as follows:

	$\overline{M_e}$ (GeV)	$\overline{M}_{\rm DA}$ (GeV)	$\overline{M}_{e+\rm jet}$ (GeV)
H1	200.8 ± 2.2(stat)	201.7 ± 5.4(stat)	203.6 ± 4.4(stat)
ZEUS	219 ± 6(stat)	229 ± 7(stat)	

Note, each of the two data samples includes, on average, 1.5 events from SM production which should be excluded before determining the average mass values. Furthermore, ZEUS has not yet given values for $M_{e+\mathrm{had}}$.

In summary, for the reasons given, it is too early to say whether the findings of the two experiments are compatible or incomaptible with the production of a single narrow mass state [6].

4.3. Charged current scattering

Results on charged current (CC) deep inelastic scattering

$$e^+ p \to \overline{\nu} X, \tag{40}$$

at large Q^2 have been presented by H1 for the 1994–96 data [59] and in preliminary form for the 1994–97 data by H1 [61,62] and ZEUS [61,62,78].

4.3.1. Event selection

The event kinematics has been reconstructed using the JB-method, see Eq. (31). The kinematic variables have been corrected for systematic effects, based on Monte Carlo simulations of the detector response to CC DIS events. The resolution in the $y - M_{\mathrm{JB}}$ plane for the H1 data is shown in Fig. 17 (bottom plot). For the ZEUS analysis the average resolution for $x_{\mathrm{JB}} > 0.3$ is 15% in x_{JB}, $\approx 20\%$ in y_{JB} and $\approx 40\%$ in Q^2_{JB}. Not surprisingly, without the detection of the scattered lepton, the determination of the kinematics for CC events is less precise than for NC events.

A key signature of high Q^2 CC events is the large missing transverse momentum, p_{Th}, which is carried away by the $\overline{\nu}$. p_{Th} can be compared with the total transverse energy observed in the detector, $E_{\mathrm{T}} = \sum_h \sqrt{p^2_{Xh} + p^2_{Yh}}$. The selection criteria applied by the two experiments are listed in Table VII.

[6] The difference between the $\overline{M}_e$ values of H1 and ZEUS is about $18 \pm 6(\mathrm{stat}) \pm 10(\mathrm{syst})$ GeV.

TABLE VII

Parameters and selection criteria for the DIS CC high Q^2 analyses

parameter	H1	ZEUS
int. luminosity (pb^{-1})	23.7	33
longt. vertex (cm)	$\lvert Z_{vtx} - Z_0 \rvert < 35$	$\lvert Z_{vtx} \rvert < 50$
tracking		≥ 1 track from VTX
minimum p_{Th} (GeV)	$p_{Th} > 50$	$p_{TH} > 15$
minimum p_{th}/E_T	0.5	0.4
minimum Q^2 (GeV^2)	2500	1000
overall efficiency		73
	N. events	N. events
$Q^2 > 1000 GeV^2$		455
$Q^2 > 2500 GeV^2$	61	

4.3.2. Prediction of the Standard Model for CC scattering

The SM cross section for CC scattering is given by Eqs (8), (24)–(27) which in LO QCD simplifies to Eq. (28). For e^+p scattering, the d quark is expected to dominate the cross section. The principal theoretical uncertainty in evaluating the SM prediction is therefore the uncertainty in $d(x, Q^2)$. The uncertainty of the predicted SM cross section was found to be 8% for $Q^2_{JB} > 1000$ GeV^2 increasing to 22% for $Q^2_{JB} > 20000$ GeV^2.

The energy scale of the calorimeter presents the main uncertainty in calculating the SM prediction; the latter grows as Q^2 increases. In the case of ZEUS, the uncertainty of the energy scale of 3% results in a systematic error of 70% on the SM expected number of events for $Q^2 = 20000 GeV^2$.

4.3.3. Background processes

There are two main sources of background for CC processes with large x and Q^2: (*i*) processes with high transverse energy in the final state (like hard photoproduction or high Q^2 NC DIS) which could result in apparent high missing transverse momentum due to detector effects; and (*ii*) production of W bosons decaying to lepton–ν. ZEUS estimates the total background for $Q^2 > 1000$ GeV^2 to amount to 3.6 events or less than 1%. For $Q^2 > 3000$ GeV^2 only the contribution from W production survives the CC selection cuts; the expected number of background events from this source decreases with x_{JB} and Q^2_{JB} similarly to the CC DIS expectations and is therefore negligible.

H1 results:
Figure 30 (top) shows the number of events as a function of Q^2_{JB}. The numbers of events observed (N_{obs}, dots) agree well with the SM predictions (N_{pred}, histogram) for Q^2_{JB} up to about 15000 GeV^2 while at higher Q^2_{JB} the data exceed the expectations somewhat (see also bottom of Fig. 30 where the ratio of observed to expected number of events is given).

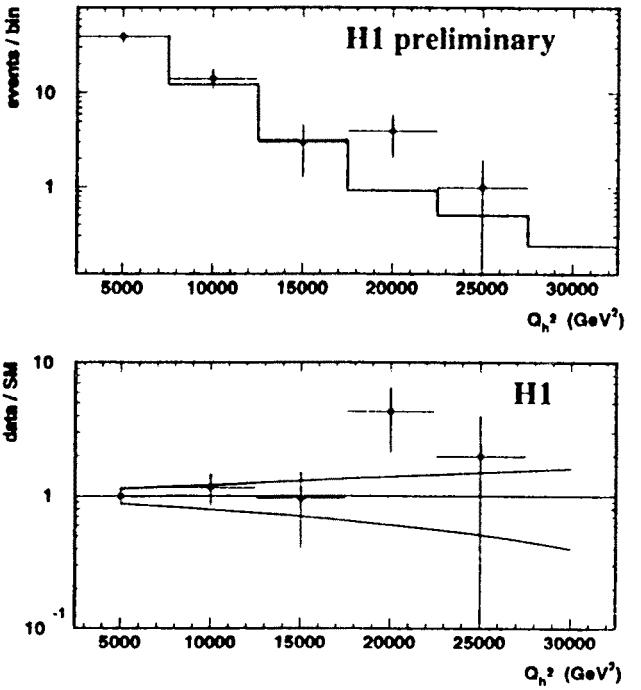

Fig. 30. Process $e^+p \to \bar{\nu}X$, results from H1: (top) Q^2_{JB} distribution of number of events observed (dots) and predicted by the SM (histogram). (bottom) Ratio of observed and expected number of events as a function of Q^2_{JB}. The lines above and below unity specify $\pm$ 1 s.d. limits for the SM prediction.

The distribution of y_{JB} versus M_{JB} is displayed in Fig. 31. There are 6 events at $Q^2_{\mathrm{JB}} > 15000$ GeV^2, $M_{\mathrm{JB}} > 150$ GeV, where about 2.9 ± 1.4 are expected.

ZEUS results:
Figure 32 shows the number of events as a function of Q^2_{JB}. The numbers of events observed (N_{obs}, dots) agree well with the SM predictions (N_{pred}, histogram) for Q^2_{JB} up to about 15000 GeV^2; for higher Q^2 there are a few events more observed than expected.

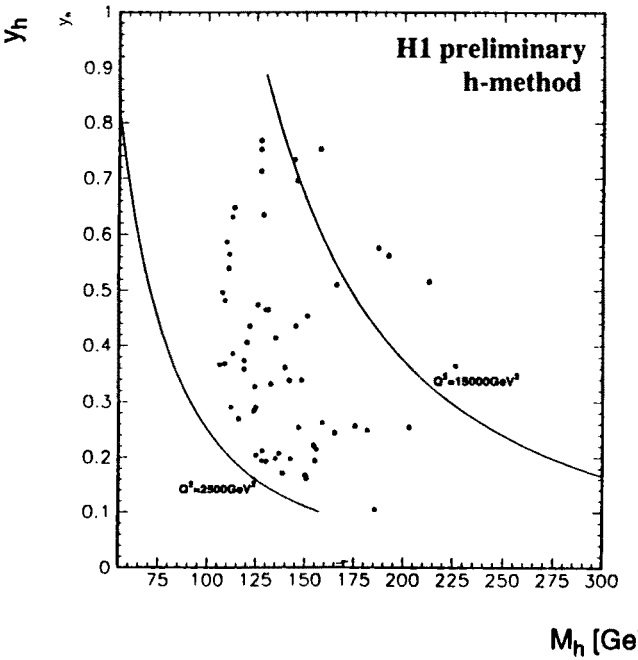

Fig. 31. Process $e^+p \to \overline{\nu}X$, results from H1: distribution of y_{JB} versus M_{JB}.

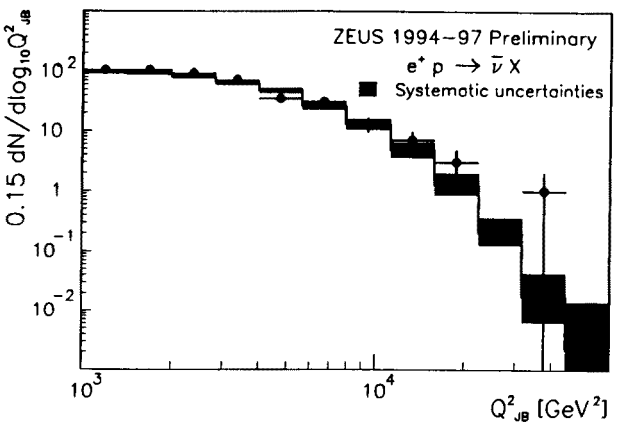

Fig. 32. Process $e^+p \to \overline{\nu}X$, results from ZEUS: Q^2_{JB} distribution of number of events observed (dots) and predicted by the SM (histogram).

Figure 33(top) shows the number of events as a function of $x_{\rm JB}$ for $Q^2_{\rm JB} > 1000$ GeV^2. The numbers of events observed ($N_{\rm obs}$, dots) agree well with the SM predictions for $x_{\rm JB} < 0.3$. For higher $x_{\rm JB}$ values more events are observed than expected:

$x_{\rm min}$(GeV^2)	$N_{\rm obs}(x_{\rm JB} > x_{\rm min})$	$N_{\rm pred}(x_{\rm JB} > x_{\rm min})$
0.1	186	$167 \pm 8.5 \pm 16$
0.2	52	$45.5 \pm 5.0 \pm 4.6$
0.3	17	$11.5 \pm 1.9 \pm 1.1$
0.4	5	$2.8 \pm 0.6 \pm 0.3$
0.5	1	$0.65 \pm 0.20 \pm 0.10$

For the SM predictions, the first (second) error gives the uncertainty due to the energy scale (due to uncertainties in the parton densities).

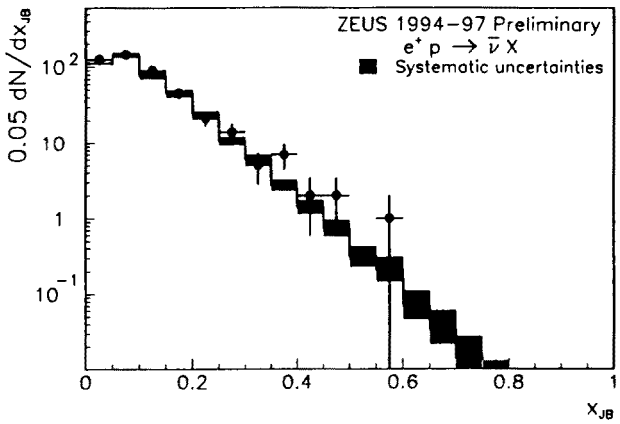

Fig. 33. Process $e^+p \to \overline{\nu}X$, results from ZEUS: $x_{\rm JB}$ distribution of number of events observed (dots) and predicted by the SM (histogram).

The distribution of $y_{\rm JB}$ versus $x_{\rm JB}$ is displayed in Fig. 34. For $Q^2_{\rm JB} > 30000$ GeV^2 there is one event observed where $0.034^{+0.037}_{-0.016} \pm 0.008$ events are expected. This particular event has $x_{\rm JB} = 0.57$ corresponding to $M_{\rm JB} = 227$ GeV.

H1 + ZEUS:

The comparison between observed and predicted number of events for the combined H1 + ZEUS data yields for $Q^2_{\rm JB} > Q^2_{JB,\rm min}$:

$Q^2_{\min}(\mathrm{GeV}^2)$	N_{obs} $Q^2_{\mathrm{JB}} > Q^2_{\min}$	N_{pred} $Q^2_{\mathrm{JB}} > Q^2_{\min}$	N_{obs} $Q^2_{\mathrm{JB}} > Q^2_{\min}$	N_{pred} $Q^2_{\mathrm{JB}} > Q^2_{\min}$
	H1		ZEUS	
1000			455	$419 \pm 13 \pm 33$
2500	61	56.3 ± 9.40		
5000	43	34.7 ± 6.90		
10000	13	8.33 ± 3.10	15	$9.4 \pm 2.5 \pm 1.6$
15000	6	2.92 ± 1.44	5	$2.0^{+0.81}_{-0.54} \pm 0.10$
20000	4	1.21 ± 0.64	1	$0.46^{+0.28}_{-0.16} \pm 0.10$
30000			1	$0.034^{+0.037}_{-0.016} \pm 0.008$

For $Q^2_{\mathrm{JB}} > 10000$ GeV^2 H1 and ZEUS together observe 28 events where 17.7 ± 4.3 are expected.

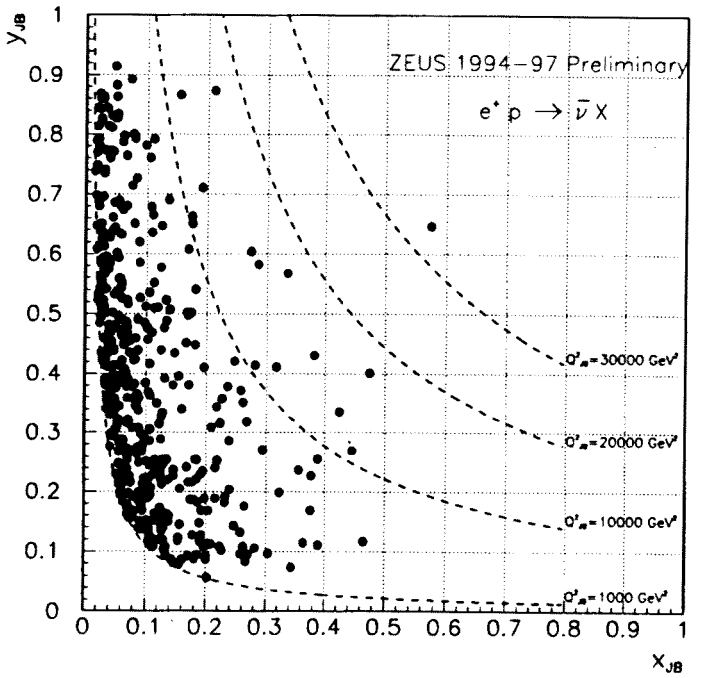

Fig. 34. Process $e^+p \to \overline{\nu}X$, results from ZEUS: distribution of y_{JB} versus x_{JB}.

4.4. Summary of the experimental results on NC and CC scattering

The experimental results on the high-Q^2, high-x can be summarized as follows:

- H1 and ZEUS have entered a new kinematical regime of deep inelastic scattering characterized by $Q^2 > 10000$ GeV^2 corresponding to a resolution of $\Delta < 2 \cdot 10^{-16}$ cm.
- Good agreement of the NC and CC results with the Standard Model is observed for $Q^2 < 15000$ GeV^2.
- The NC data exhibit an excess of events over the SM predictions for $Q^2 > 15000$ GeV^2. The probability that the excess seen in the combined H1+ZEUS data is consistent with the SM is at the 0.2% to 1% level.
- The NC excess is concentrated at large values of x (large M).
- The NC excess cannot be accounted for by detector effects or by non-DIS background.
- A failure of the SM seems unlikely, see [59,60,79–82].
- The data do not exclude a single narrow resonance as the origin of the excess.
- Although the probability is small, it is not excluded that the excess is the result of statistical fluctuations.
- The CC data show a tendency to lie above the SM predictions for large Q^2_{JB} and large x_{JB}.

4.5. Mechanisms beyond the Standard Model

The excess in NC scattering has stimulated an intense discussion on whether the HERA events could be the sign for New Physics. It has been noted that the presence or absence of a similar excess in CC scattering will severly limit the number of possible interpretations, see *e.g.* [79,85]. Recent summaries can be found in [86–88]. It is beyond the scope of this report to give a detailed account; rather, a few selected mechanisms for new physics will be compared with the data.

4.5.1. Contact interactions

If leptons and quarks are composite objects they may have common constituents which give rise to additional interactions. In the low energy approximation these as well as the exchange of heavy particles (with masses

in the TeV range) can be described by contact interactions. The most general chiral invariant neutral current contact interaction Lagrangian can be written in the form [89–91]:

$$\mathcal{L} = 4\pi \sum_{q=u,d;\ i,j=L,R} \frac{\eta_{ij}^{eq}}{(\Lambda_{i,j}^{eq})^2} (\overline{e_i}\gamma^\mu e_i)(\overline{q_j}\gamma_\mu q_j) \tag{41}$$

where Λ_{ij}^{eq} is the mass scale and η_{ij}^{eq} the relative size and sign of the individual terms. By convention, the strength of the interaction is assumed to be $g^2/4\pi = 1$, and $|\eta| = 1$ when quoting limits on Λ_{ij}^{q}.

Contact interactions as a possibility to explain the excess observed at large Q^2 have been discussed in [92–100]. Severe constraints on contact interactions are placed by the experimental limits on atomic parity violation (APV) (see *e.g.* [101, 102]). The difference between the measurement and the SM prediction on APV in $^{133}_{55}$Cs yields [94]: $\Delta Q_W = 1.0 \pm 0.93$ and constrains the contact interaction to [83, 84, 94]:

$$\begin{aligned} \Delta Q_W \;=\; & 143\left(\frac{\eta_{LL}^{eu}}{(\Lambda_{LL}^{eu})^2} + \frac{\eta_{LR}^{eu}}{(\Lambda_{LR}^{eu})^2} - \frac{\eta_{RL}^{eu}}{(\Lambda_{RL}^{eu})^2} - \frac{\eta_{RR}^{eu}}{(\Lambda_{RR}^{eu})^2}\right) \\ & +161\left(\frac{\eta_{LL}^{ed}}{(\Lambda_{LL}^{ed})^2} + \frac{\eta_{LR}^{ed}}{(\Lambda_{LR}^{ed})^2} - \frac{\eta_{RL}^{ed}}{(\Lambda_{RL}^{ed})^2} - \frac{\eta_{RR}^{ed}}{(\Lambda_{RR}^{ed})^2}\right), \end{aligned} \tag{42}$$

where the Λ's are measured in units of TeV.

If contact interactions contribute only to a single flavor/helicity combination, the corresponding Λ value must be above 10 TeV according to the APV constraint. However, the APV constraint can also be satisfied by a judicious combination of several terms. For instance, parity conserving contact interactions such as

$$\frac{\eta_{LR}^{eq}}{(\Lambda_{LR}^{eq})^2} = \frac{\eta_{RL}^{eq}}{(\Lambda_{RL}^{eq})^2} \quad \text{and} \quad \frac{\eta_{LL}^{eq}}{(\Lambda_{LL}^{eq})^2} = \frac{\eta_{RR}^{eq}}{(\Lambda_{RR}^{eq})^2}$$

give $\Delta Q_W = 0$. In e^+p interactions LL and RR contributions are suppressed by a factor $(1-y)^2$ in comparison with the LR and RL ones [103]. For e^-p scattering the opposite holds. The sum of the contributions from the SM and the contact interactions is of the form $\sigma_{SM} + a\frac{Q^2}{\Lambda^2} + b\frac{Q^4}{\Lambda^4}$ where the second term describes the interference between the two processes.

The HERA data can be reproduced approximately with the combination $(LR + RL)$ for $\Lambda^{+u} = 4TeV$ [104] as shown in Fig. 35, see also [94].

Note the data point at $Q^2_{\text{min}} = 10^4$ GeV^2 which is pulling the contribution from the contact interaction down and pushing the value of Λ up.

The presence of contact interactions can also be probed by e^+e^- annihilation and $p\bar{p}$ interactions. The lower limit on Λ^{+u} obtained by OPAL

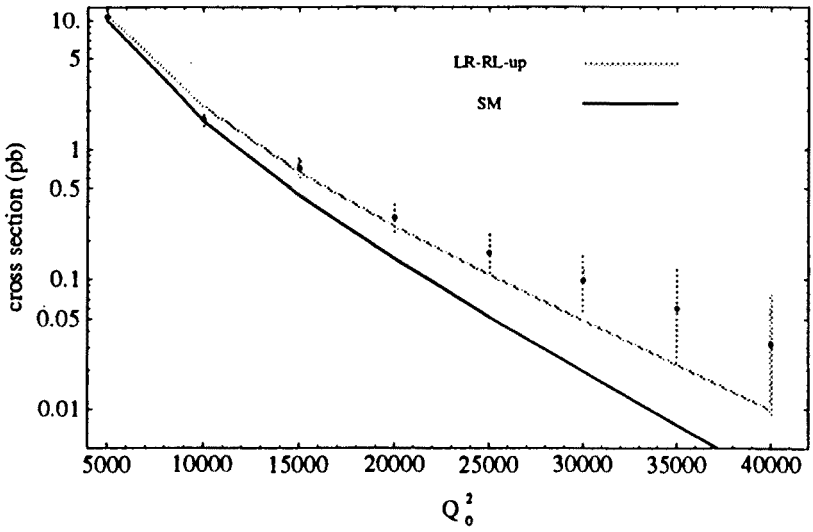

Fig. 35. The NC cross section from the combined H1 and ZEUS data for $Q^2 > Q^2_{\min}$ as a function of $Q^2_{\min}$. The solid curve shows the SM contribution; the addition of a contact interaction of the type $LR + RL$ with $\Lambda = 4$ TeV yields the dotted curve. (Update of figure presented by [104], from [86]).

(e^+e^-) is 2 TeV, while that from CDF $(p\overline{p})$ is 2.7 TeV [86]; both limits are compatible with the HERA data. Contact interactions are expected to contribute to e^+p as well as e^-p NC interactions but not to CC interactions [85] because one of the two terms (LR or RL) will vanish, violating the APV and/or low energy (from π and K decays) constraints, unless Λ is very large.

4.5.2. Leptoquark production

The existence of leptoquarks (LQ) has first been discussed by [105]. Electron-proton scattering is particularly well suited for the search of leptoquarks since LQ's can be produced in the s-channel [90,106]. A classification of LQ states which takes ino account $SU(3)_c$ x $SU(2)_L$ x U(1) invariance, lepton and baryon number conservation and chirality of the couplings has been given in [107]. A recent review of leptoquarks can be found in [108]. The Born cross section for LQ production by s-channel ep scattering can be written as [107] follows [7].

[7] Leptoquarks can contribute to ep scattering also via u-channel exchange. The absence of an excess in the e^-p data excludes the possibility that the excess seen in e^+p scattering results mainly from u-channel exchange [83].

For a scalar LQ:

$$\frac{d\sigma(ep \to LQ)}{dxdy} = \frac{1}{32\pi} q(x,y) \frac{\lambda^4 xs}{(xs - M_{LQ}^2)^2 + M_{LQ}^2 \Gamma_{LQ}^2} \tag{43}$$

and for a vector LQ:

$$\frac{d\sigma(ep \to LQ)}{dxdy} = \frac{1}{8\pi} q(x,y)(1-y)^2 \frac{\lambda^4 xs}{(xs - M_{LQ}^2)^2 + M_{LQ}^2 \Gamma_{LQ}^2}, \tag{44}$$

where $q(x,y)$ is the density of quark q in the proton, $M_{LQ} = xs$ and Γ_{LQ} are the LQ mass and width, and λ measures the eq coupling strength for a particular combination of the e and q helicities. The cross section is given for unpolarized beams. The scaling variable y measures directly the angle θ^* between the incoming and outgoing e (q) in the LQ rest system:

$$y = \frac{1 - \cos\theta^*}{2}. \tag{45}$$

Note, for a scalar LQ the y distribution is uniform while for a vector LQ it is peaked at $y = 0$. Since the excess observed by H1 and ZEUS extends to large y the scalar interpretation is favored. Furthermore, CDF [109] and D0 [110], from $p\bar{p}$ interactions, provide strong lower limits on the mass of a vector LQ which make the vector hypothesis unlikely. For these reasons, only the scalar LQ solution will be discussed.

The LQ width can be expressed in terms of the eq coupling constant λ:

$$\Gamma = \frac{1}{16\pi} \lambda^2 M_{LQ}. \tag{46}$$

The size of the cross section observed for the excess limits λ and therefore the LQ width, $\Gamma \ll 1$ GeV. This permits to use the narrow width approximation for the total production cross section,

$$\frac{\sigma(ep \to LQ)}{dy} = \frac{\pi}{4s} \lambda^2 q(x,y). \tag{47}$$

QCD corrections from gluon radiation, gluon splitting and vertex corrections increase the cross section [111,112]: for $M_{LQ} = 210$ GeV the increase is about 25% compared to the Born value [8]. The cross section for LQ production and decay into a specific final state is obtained from Eq. (47) by multiplication with the branching ratio B.

[8] Note, gluon radiation from the final state quark increases the mass of the hadron system from LQ decay, see also [114, 115].

We shall assume that the H1 and ZEUS data are compatible with the production of a single narrow width LQ of mass $M_{LQ} = 210$ GeV. The combined excess from H1 and ZEUS, corrected for detection efficiency and y acceptance, corresponds to a cross section of about 0.4 ± 0.2pb. This leads to the following estimates for λ and the total width Γ [9]:

$$\begin{array}{lll} e^+u \to LQ \to e + \text{had} & \lambda_{eu} \approx 0.02 \pm 0.004/\sqrt{B} & \Gamma = 1.6 \pm 0.6\text{MeV}/B\,, \\ e^+d \to LQ \to e + \text{had} & \lambda_{ed} \approx 0.04 \pm 0.01/\sqrt{B} & \Gamma = 7.6 \pm 2.8\text{MeV}/B\,, \\ e^+s \to LQ \to e + \text{had} & \lambda_{es} \approx 0.2 - 0.4/\sqrt{B} & \Gamma = 400 \pm 200\text{MeV}/B\ . \end{array}$$

For $B = 1$ the $\lambda_{eu}, \lambda_{ed}$ are an order of magnitude smaller than $e = \sqrt{4\pi\alpha} = 0.30$ while λ_{es} is of comparable size.

APV data impose the following limits [85]: $\lambda_{e^+u} \leq 0.058$ and $\lambda_{e^+d} \leq 0.055$.

Leptoquarks can be pair-produced in $p\overline{p}$ collisions by strong interactions. The production rate depends on the gauge coupling (*i.e.* on α_s) and not on λ. No signal in the $LQ \to eq$ decay mode has been observed by CDF and D0. Assuming $B = 1$ they provide lower limits of $M_{LQ} > 210$ GeV (CDF), 225 GeV (D0) and 240 GeV for the combined CDF + D0 data, and, together with the HERA results, limit the branching ratio to $B_{eq} < 0.5$–0.7 for scalar leptoquarks of $M_{LQ} = 200$–210 GeV [86].

In e^+e^- annihilation LQ's can be exchanged in the t or u-channel. OPAL and ALEPH have measured upper limits of $|\lambda| < 0.6$–0.7 for $B = 1$ [86]; this places a significant upper limit on λ_{e^+s}.

Note, an e^+u leptoquark cannot decay into $\overline{\nu}q$ since it has charge 5/3. It will therefore not contribute to s-channel production in CC scattering. Also e^+d and e^+s leptoquarks cannot contribute to s-channel CC production provided they have SU(2) symmetric couplings [88, 107].

As shown, the available data do not exclude the possibility that the excess seen by H1 and ZEUS is due to the production of a leptoquark of composition e^+q, $q = u, d$. Such leptoquarks have fermion number $F = 0$. The explanation of the excess in terms of $F = 2$ leptoquarks, *i.e.* $LQ = e^+\overline{q}$, can be excluded on several accounts: the u, d densities of the proton at x around 0.5 are much larger than those for $\overline{u}, \overline{d}$ (see Fig. 18). If the observed excess were due to $e^+\overline{u}$ H1 and ZEUS should have observed an excess of 30–40 events in their combined e^-p NC data which is not the case [83], see Figs 13, 14. Furthermore, low energy results (APV, π, K decays) put stringent limits on the coupling strengths $\lambda_{e^-u}, \lambda_{e^-d}, \lambda_{e^-s}$ and therefore also on $\lambda_{e^+\overline{u}}, \lambda_{e^+\overline{d}}, \lambda_{e^+\overline{s}}$. The last one excludes also the combination e^+s, since the s and $\overline{s}$ densities in the proton are the same.

[9] An explanation of the excess in e^+p scattering in terms of LQ production on $\overline{u}$ or $\overline{d}$ is ruled out since it would require a large excess contribution to e^-p scattering which would be in contradiction with the data [83].

In conclusion, if the excess seen in e^+p NC scattering is due to the production of a standard leptoquark no excess is expected for e^-p NC scattering. An excess may occur in e^+p CC scattering if the observed signal is to due an e^+d state and SU(2) is violated, see *e.g.* [79,85].

4.5.3. Production of SUSY quarks

Squarks can be produced by e^+d fusion provided R-parity (where $R = (-1)^{3B+L+2S}$, B, L = baryon and lepton numbers, S = spin; $R = +1$ for standard particles, $R = -1$ for supersymmetric particles) is broken,

$$e^+d \to \tilde{u}, \tilde{c}, \tilde{t} \to eq'. \tag{48}$$

APV experiments put stringent limits on the $e\tilde{q}q'$ vertices. Only the processes $e_R^+ d_R \to \tilde{q}_L$ survive the low energy limits. Denoting the coupling for the $(lepton_i \tilde{q}_j q_k)$ vertex by λ'_{ijk} where i, j, k are generation indices, one finds from the absence of neutrinoless double β decays [92,116]:

$$|\lambda'_{111}| \leq 0.007 (\frac{M_{\tilde{q}}}{210\,\mathrm{GeV}})^2 (\frac{m_{\tilde{g}}}{1\,\mathrm{TeV}})^{0.5}, \tag{49}$$

where M_q is the mass of the lighter of $\tilde{u}_L, \tilde{d}_L$ and $m_{\tilde{g}}$ is the mass of the gluino. This excludes the process $e^+d \to \tilde{u}_L$.

APV yields also the limit

$$|\lambda'_{1j1}| \leq 0.052 \frac{M_{\tilde{q}}}{210\,\mathrm{GeV}}, \quad j = 1, 2, 3. \tag{50}$$

which by comparison with the H1+ZEUS result requires $B_{eq} > 0.25$. With the restrictions given by Eqs (49), (50) possible channels are $e_R^+ d_R \to \tilde{c}_L, \tilde{t}_L$ and $e^+s \to \tilde{t}_L$. Note, that in the presence of R-violating *and* R-conserving decays $B_{eq} < 1$.

The $\tilde{t}$ can be exchanged in e^+e^- annihilation and contribute to $e^+e^- \to s\bar{s}$ production. From the study of this channel ALEPH and OPAL find the following limit, $|\lambda_{132}| < 0.6$ - 0.7. When combined with the H1+ZEUS data one obtains the limit $B_{es} > 0.4$.

It is interesting to note that due to mixing and to the large mass of the top quark, two heavy mass eigenstates $\tilde{t}_1, \tilde{t}_2$ may exist at masses around 200 GeV [117].

The question whether the existing strong experimental bounds on flavor changing neutral currents (FCNC) can be accomodated in SUSY together with the presence of R-parity violations as suggested by the HERA data in a consistent manner has been studied in [118] and answered affirmatively.

4.6. Conclusions

The excess of events observed by H1 and ZEUS at $Q^2 > 15000$ GeV^2 and $x > 0.4$ is very intriguing. The results are not yet statistically compelling and more data are needed. Also, work is in progress to improve the reconstruction of the mass of the e-had system. The excess events may be the first sign of a new layer of physics.

I want to thank the organizers of the School for a highly spirited meeting and for their the warm hospitality. I am grateful to Dr. H. Spiesberger for very helpful discussions on the theoretical interpretation of the high-x, high-Q^2 excess seen by H1 and ZEUS.

REFERENCES

[1] HERA, A Proposal for a Large Electron-Proton Colliding Beam Facility at DESY, DESY HERA 81-10(1981); B.H. Wiik, Electron-Proton Colliding Beams, The Physics Programme and the Machine, Proc. 10^{th} SLAC Summer Institute, ed. A. Mosher, 1982, p. 233; Proc. XXVI Int. Conf. High Energy Physics, Dallas, 1992; G.A. Voss, Proc. First Euro Acc. Conf., Rome, 1988, p. 7.

[2] H1 Collaboration, Technical Proposal for the H1 Detector, 1986; The H1 Detector at HERA, H1 Collaboration, I. Abt *et al.*, DESY 93-103 (1993) and *Nucl. Inst. Meth.* **A386**, 310, 348 (1997).

[3] ZEUS Collaboration, The ZEUS Detector, Technical Proposal, 1986; The ZEUS Detector, Status Report 1993, ed. U. Holm; A brief description of the detector can be found in [4].

[4] G. Wolf, HERA Physics, DESY 94-022 (1994) and Proc. 42nd Scottish Universities Summer School in Physics, 1993.

[5] HERMES Collaboration, HERMES, Technical Design Report, 1993.

[6] HERA-B Collaboration, HERA-B: An Experiment to Study CP Violation in the B System Using an Internal Target at the HERA Proton Ring, DESY-PRC 94/02, 1994.

[7] H1 Collaboration, S. Aid *et al.*, DESY 96-039 (1996).

[8] ZEUS Collaboration, M. Derrick *et al.*, *Z. Phys.* **C69**, 607 (1996).

[9] ZEUS Collaboration, M. Derrick *et al.*, *Z. Phys.* **C72**, 399 (1996).

[10] BCDMS Collaboration, A.C. Benvenuti *et al.*, *Phys. Lett.* **B223**, 490 (1989).

[11] E665 Collaboration, M.R. Adams *et al.*, FERMILAB-PUB-95-396-E.

[12] NMC Collaboration, M. Arneodo *et al.*, *Phys. Lett.* **B364**, 107 (1995).

[13] L.W. Whitlow *et al.*, *Phys. Lett.* **B282**, 475 (1992).

[14] V.N. Gribov, L.N. Lipatov, *Sov. J. Nucl. Phys.* **15**, 438, 675 (1972); L.N. Lipatov, *Sov. J. Nucl. Phys.* **20**, 95 (1975); Yu.L.Dokshitzer, *Sov. Phys. JETP* **46**, 641 (1977); G. Altarelli, G. Parisi, *Nucl. Phys.* **B126**, 298 (1977).

[15] H1 Collaboration, C. Adloff *et al.*, DESY 96-236 (1996).

[16] A.D. Martin, W.J. Stirling, R.G. Roberts, *Phys. Lett.* **B306**, 145 (1993); erratum *Phys. Lett.* **309**, 492 (1993).

[17] H1 Collaboration, C. Adloff *et al.*, DESY 96-138 (1996).

[18] ZEUS Collaboration, M. Derrick *et al.*, report in preparation.

[19] M. Glück, E. Reya, M. Stratmann, *Nucl. Phys.* **422**, 37 (1994).

[20] M. Glück, E. Reya, A. Vogt, *Z. Phys.* **C67**, 433 (1995); references to earlier work can be found there.

[21] E. Laenen, S. Riemersma, J. Smith, W.L. Van Neerven, *Nucl. Phys.* **B392**, 162 (1993); S. Riemersma, J. Smith, W.L. Van Neerven, *Phys. Lett.* **B347**, 147 (1995); E. Laenen *et al.*, Proc. Workshop "Future Physics at HERA", DESY, Hamburg, Vol.1 (1995/96) p. 393; K. Daum *et al.*, Proc. Workshop "Future Physics at HERA", DESY, Hamburg, p. 89.

[22] We follow here J. Kwiecinski, *Substructures of Matter as revealed with Electroweak Probes*, Proc. Schladming,1993, eds. L.Mathelitsch, W. Plessas, Lecture Notes in Physics 426, Springer Verlag, p.215.

[23] C. Lopez, F.J. Yndurain, *Nucl. Phys.* **B171**, 231 (1980); *Phys. Rev. Lett.* **44**, 1118 (1980).

[24] See *e.g.* E. Leader, E. Predazzi, *An Introduction to Gauge Theories and the New Physics*, Cambridge U.P., Cambridge 1982; R.G. Roberts, *The Structure of the Proton*, Cambridge U.P., Cambridge 1990.

[25] For a nonasymptotically free vector theory: V.N. Gribov, L.N. Lipatov, *Yad. Fiz.* **15**, 781 (1972); *Sov. J. Nucl. Phys.* **15**, 438 (1972).

[26] For an asymptotically free vector theory: A. De Rujula *et al.*, *Phys. Rev.* **D10**, 1649 (1974).

[27] L.N. Lipatov, *Sov. J. Nucl. Phys.* **23**, 338 (1976); Y.Y. Balitsky, L.N. Lipatov, *Sov. J. Nucl. Phys.* **28**, 822 (1978); E.A. Kuraev, L.N. Lipatov, V.S. Fadin, *Sov. Phys. JETP* **45**, 199 (1977).

[28] G. Bottazzi, G. Marchesini, G.P. Salam, M. Scorletti, IFUM 552-FT (1997) and hep-ph/9702418.

[29] See also M. Scorletti, IFUM 574-FT (1997) and hep-ph/9707237.

[30] See also S. Catani, XVIII Int. Symp. Lepton Photon Interactions, 1997, Hamburg.

[31] J. Kwiecinski, A.D. Martin, A.M. Staśto, hep-ph/9706455 (1997).

[32] A.D. Martin, W.J. Stirling, R.G. Roberts, *Phys. Rev.* **D50**, 6734 (1994).

[33] R. Brock *et al.*, *Rev. Mod. Phys.* **67**, 157 (1995).

[34] C. Lopez, F. Barreiro, F.J. Yndurain, DESY 96-087 (1996).

[35] R.D. Ball, R.D. Forte, *Phys. Lett.* **B335**, (1994) 77; CERN-TH/95-323 (1995).

[36] For a recent analysis see W. Buchmüller, D. Haidt, DESY 96-061 (1996).

[37] D. Haidt, preprint, 1997.

[38] L.N. Hand, *Phys. Rev.* **129**, 1834 (1963); S.D. Drell, J.D. Walecka, *Ann. Phys.* (N.Y.) **28**, 18 (1964); F.J. Gilman, *Phys. Rev.* **167**, 1365 (1968).

[39] B.L. Ioffe, *Phys. Lett.* **30**, 123 (1969); B.L. Ioffe, V.A. Khoze, L.N. Lipatov, *Hard Processes*, North Holland, 1984, p.185.

[40] ZEUS Collaboration, M. Derrick *et al.*, *Z. Phys.* **C65**, 379 (1995).

[41] ZEUS Collaboration, J. Breitweg *et al.*. DESY 97-153 (1997) and hep-ex/9707025.

[42] ZEUS collaboration, paper submitted to the XXVIII Int. Conf. High Energy, Warsaw, 1996.

[43] H1 Collaboration, I. Abt *et al.*, DESY 97-042 (1997) and hep-ex/970312.

[44] E665 Collaboration, M.R. Adams *et al.*, *Phys. Rev.* **D54**, 3006 (1996).

[45] A. Donnachie, P.V. Landshoff, *Z. Phys.* **C61**, 139 (1994).

[46] A. Capella *et al.*, *Phys. Lett.* **B337**, 358 (1994).

[47] B. Badelek, J. Kwiecinski, *Rev. Mod. Phys.* **68**, 445 (1996).

[48] M. Glück, E. Reya, A. Vogt, *Z. Phys.* **C67**, 433 (1995).

[49] K. Adel, F. Barreiro, F.J. Yndurain, FTUAM 96-39 and DESY 97-088 (1997).

[50] For a discussion see also A. Levy, Proc. Workshop Deep Inelastic Scattering, Rome 1996, ed. A. Negri and G. D'Agostini, and DESY 97-013 (1997).

[51] E. Derman, *Phys. Rev.* **D7**, 2755 (1973); G. Ingelman, R. Rueckl, *Phys. Lett.* **B201**, 369 (1988).

[52] H1 Collaboration, T. Ahmed *et al.*, *Phys. Lett.* **B324**, 241 (1994); S. Aid *et al.*, *Z. Phys.* **C67**, 565 (1995).

[53] H1 Collaboration, S. Aid *et al.*, Phys.Lett. **B379**, 319 (1996).

[54] ZEUS Collaboration, M. Derrick *et al.*, *Phys. Rev. Lett.* **75**, 1006 (1995).

[55] ZEUS Collaboration, M. Derrick *et al.*, *Z. Phys.* **C72**, 47 (1996).

[56] ZEUS Collaboration, preliminary results, unpublished.

[57] Particle Data Group, *Phys. Rev.* **D54**, 1 (1996).

[58] Future Physics at HERA, ed. G. Ingelman, A. DeRoeck and R. Klanner, DESY, Hamburg 1996), and references therein; R. Cashmore *et al.*, *Phys. Rep.* **122**, 275 (1985).

[59] H1 Collaboration, C. Adloff *et al.*, *Z. Phys.* **C74**, 191 (1997).

[60] ZEUS Collaboration, J. Breitweg *et al.*, *Z. Phys.* **C74**, 207 (1997).

[61] B. Straub, New Results on Neutral and Charged Current Scattering at High Q^2 from H1 and ZEUS, XVIII Int. Symp. Lepton Photon Interactions, 1997, Hamburg.

[62] E. Elsen, New High Q^2 Results in ep Collisions at HERA, EPS High Energy Physics Conference, 1997, Jerusalem.

[63] F. Jacquet, A. Blondel, Proc. Study of an ep Facility in Europe, ed. U. Amaldi, 79/48, p.391.

[64] S. Bentvelsen, J. Engelen,, P. Kooijman, Proceedings of the Workshop on Physics at HERA, ed. W. Buchmüller and G. Ingelman, DESY (1992) Vol.1, 23.

[65] K.C. Hoeger, Proceedings of the Workshop on Physics at HERA, ed. W. Buchmüller and G. Ingelman, DESY (1992) Vol.1, 43.

[66] V.N. Gribov, L.N. Lipatov, *Sov. J. Nucl. Phys.* **15**, 438, 675 (1972); Y. Dokshitzer, *Sov. Phys. JETP* **46**, 641 (1977); G. Altarelli, G. Parisi, *Nucl. Phys.* **126**, 297 (1977).

[67] G. Altarelli, G. Martinelli, *Phys. Lett.* **B76**, 89 (1978).

[68] J. Timmermans, XVIII Int. Symp. Lepton Photon Interactions, 1997, Hamburg.

[69] A.D. Martin, R.G. Roberts, W.J. Stirling, Durham Univ. preprint DTP-93-86 and RAL-93-077 (1993); Proc. Workshop Quantum Field Aspects of High Energy Physics, ed. B. Geyser and E.M. Ilgenfritz (1993), p.11.

[70] H. Plothow-Besch, PDFLIB User's Manual, version 7.07, W5051 PDFLIB, 1996.12.09, CERN-PPE, and references given therein; *Int. J. Mod. Phys.* **A10**, 2901 (1995).

[71] NMC Collaboration,M. Arneodo *et al.*, *Phys. Lett.* **B309**, 222 (1993) and references therein.

[72] CCFR Collaboration, P.Z. Quintas *et al.*, *Phys. Rev. Lett.* **71**, 1307 (1993).

[73] HERACLES 4.5.2: A. Kwiatkowski, H. Spiesberger, H.-J. Möhring, *Z. Phys.* **C50**, 165 (1991).

[74] A. Arbuzov *et al.*, DESY 95-185 (1995).

[75] G. Wolf, DESY 97-047 (1997) and hep-ex/9704006 (1997), extended version.

[76] U. Bassler, G. Bernardi, DESY 97-136 (1997).

[77] S. Jadach, W. Plazek, B.F.L. Ward, UTHEP-97-0103 (1997) and hep-ph/9705395.

[78] ZEUS Collaboration, EPS High Energy Physics Conference, 1997, Jerusalem, paper N-686.

[79] K.S. Babu, C. Kolda, J. March-Russel, IASSNS-HEP 97-55 (1997) and hep-hp/9705399.

[80] J.F. Gunion, R. Vogt, UCD-97-14 (1997) and hep-ph/9706252 (1997).

[81] W. Melnitchouk, A.W. Thomas, hep-ph/9707387 (1997).

[82] S. Rock, P. Bosted, Report hep-ph/9706436 (1997).

[83] K.S. Babu, C. Kolda, J. March-Russell, F. Wilczek, IASSNS-HEP-97-04 (1997)and hep-ph/9703299.

[84] A. Deandrea, *Phys. Lett.* **B409**, 277 (1997).

[85] G. Altarelli, G.F. Giudice, M.L. Mangano, CERN-TH/97-101 (1997) and hep-ph/9705287.

[86] G. Altarelli, *The Status of the Standard Model*, XVIII Int. Symp. Lepton Photon Interactions, 1997, Hamburg, CERN-TH/97-278 (1997) and hep-ph/9710434.

[87] J. Ellis, rapporteur talk presented at the EPS High Energy Physics Conference, 1997, Jerusalem.

[88] R. Rückl, H. Spiesberger, BI-TP 97/40, MPI-PhT/97-63,WUE-ITP-97-040 and hep-ph/9710327 (1997), and H. Spiesberger, talk presented at the Workshop on HERA Physics, Korean Detector Laboratory, October 1997.

[89] E. Eichten, K. Lane, M.E. Peskin, *Phys. Rev. Lett.* **50**, 811 (1983).

[90] P. Haberl, F. Schrempp, H.-U. Martyn, Proc. Workshop "Physics at HERA", eds. W. Buchmüller and G. Ingelmann, DESY, Hamburg (1991), vol.2, p.113.

[91] K. Akama, H. Terazawa, *Mod. Phys. Lett.* **A9**, 3423 (1994); H. Terazawa, Univ. Tokyo INS-1146(1996); K. Akama, K, Katsuura, H.Terazawa, KEK 97-7 (1997) and hep-ph/9704327.

[92] G. Altarelli, J. Ellis, G.F. Giudice, S. Lola, M.L. Mangano, CERN-TH/97-40 (1997) and hep-ph/9703276.

[93] J. Blumlein, DESY 97-032 (1997) and hep/ph/9703287.

[94] V. Barger, K. Cheung, K. Hagiwara, D. Zeppenfeld, MADPH-97-991 (1997) and hep-ph/9703311. D. Zeppenfeld, MADPH-97-1001 (1997) and hep-ph/9706357. V. Barger, K. Cheung, K. Hagiwara, D. Zeppenfeld, MADPH-97-999, DOE-ER40757-100, KEK-TH-529 and hep-ph/9707412. V. Barger, K. Cheung, D.P. Roy, D. Zeppenfeld, MADPH-97-1015, UCD-97-23 (1997) and hep-ph/9710353.

[95] J. Kalinowski, R. Rückl, H. Spiesberger, P.M. Zerwas, DESY 97-044 (1997) and hep-ph/9703436.

[96] W. Buchmüller, D. Wyler, DESY 97-066 and ZU-TH/ 9/97 (1997).

[97] S. Barshay, G. Kreyerhoff, PITH 97/15 (1007) and hep-ph/9705303.

[98] P.H. Frampton, Report hep-ph/9706220 (1997).

[99] F. Caravaglios, CERN-TH/97-104 (1997) and hep-ph/9706288.

[100] L. Giusti, A. Strumia, IFUP-TH/23-97 (1997) and hep-ph/9706298.

[101] S. Davidson, D. Bailey, B.A. Campbell, *Z. Phys.* **C61**, 613 (1994).

[102] C.S. Wood *et al.*, *Science* **275**, 1759 (1997).

[103] D. Zeppenfeld, 5th Int. Workshop Depp Inelastic Scattering and QCD, Chicago, Illinois, 1997, and hep-ph/9706357.

[104] N. DiBartolomeo, M. Fabbrichesi, results quoted in [86].

[105] J.C. Pati, A. Salam, *Phys. Rev.* **D8**, 1240 (1973); *Phys. Rev. Lett.* **31**, 661 (1973); *Phys. Rev.* **D10**, 275 (1974).

[106] R.J. Cashmore *et al.*, *Phys. Rep.* **122**, 275 (1985).

[107] W. Buchmüller, R. Rückl, D. Wyler, *Phys. Lett.* **B191**, 442 (1987).

[108] J. L. Hewett, T.G. Rizzo, *Phys. Rev.* **D56**, 5709 (1997).

[109] CDF Collaboration, data quoted by Altarelli.

[110] D0 Collaboration, data quoted by Altarelli.

[111] Z. Kunszt, W.J. Stirling, *Z. Phys.* **C75**, 453 (1997).

[112] T.Plehn, H. Spiesberger, M. Spira, P. Zerwas, *Z. Phys.* **C74**, 611 (1997).

[113] I. Montvay, DESY 97-058 (1997).

[114] C. Friberg, E. Norrbin, T. Sjöstrand, LU-TP 97-04 (1997) and hep-ph/9704214.

[115] M. Heyssler, W.J. Stirling, hep-ph/9705229 (1997).

[116] M. Hirsch, H.V. Klapdor-Kleingrothaus, S.G. Kovalenko, *Phys. Rev. Lett.* **75**, 17 (1995), and *Phys. Rev.* **D53**, 4445 (1995).

[117] T. Kobayashi, S. Kitamura, T. Kon, *Int. J. Mod. Phys.* **A11**, 1875 (1996). T. Kon, Matsushita, T. Kobayashi, hep-ph/9707355 (1997).

[118] R. Barbieri *et al.*, hep-ph/9704275 (1997).